

# Journal of Geophysical Research: Earth Surface

## RESEARCH ARTICLE

10.1002/2014JF003171

**Key Points:**

- Lagrangian processing of satellite altimetry improves elevation change detection
- Basal mass budgets are derived for the Ross and Filchner-Ronne Ice Shelves
- The ice shelf frontal zones provide large fractions of the total basal mass loss

**Supporting Information:**

- Readme
- Text S1

**Correspondence to:**G. Moholdt,  
moholdt@npolar.no**Citation:**

Moholdt, G., L. Padman, and H. A. Fricker (2014), Basal mass budget of Ross and Filchner-Ronne ice shelves, Antarctica, derived from Lagrangian analysis of ICESat altimetry, *J. Geophys. Res. Earth Surf.*, 119, 2361–2380, doi:10.1002/2014JF003171.

Received 8 APR 2014

Accepted 30 SEP 2014

Accepted article online 1 OCT 2014

Published online 7 NOV 2014

## Basal mass budget of Ross and Filchner-Ronne ice shelves, Antarctica, derived from Lagrangian analysis of ICESat altimetry

**Geir Moholdt<sup>1,2</sup>, Laurie Padman<sup>3</sup>, and Helen Amanda Fricker<sup>1</sup>**

<sup>1</sup>Institute of Geophysics and Planetary Physics, Scripps Institution of Oceanography, La Jolla, California, USA, <sup>2</sup>Norwegian Polar Institute, Tromsø, Norway, <sup>3</sup>Earth & Space Research, Corvallis, Oregon, USA

**Abstract** Traditional methods of deriving temporal variability of Antarctic ice-shelf elevation from satellite altimetry use a fixed (“Eulerian”) reference frame, where the measured changes include advection of ice thickness gradients between measurement epochs. We present a new method which removes advection effects by using an independent velocity field to compare elevations in a moving (“Lagrangian”) reference frame. Applying the technique to ICESat laser altimetry for the period 2003–2009 over the two largest Antarctic ice shelves, Ross and Filchner-Ronne, we show that the Lagrangian approach reduces the variability of derived elevation changes by about 50% compared to the Eulerian approach and reveals clearer spatial patterns of elevation change. The method simplifies the process of estimating basal mass budget from the residual of all other processes that contribute to ice-shelf elevation changes. We use field data and ICESat measurements over ice rises and the grounded ice sheet to account for surface accumulation and changes in firn air content, and remove the effect of ice-flow divergence using surface velocity and ice thickness data. The results show highest basal melt rates ( $>5 \text{ m a}^{-1}$ ) near the deep grounding lines of major ice streams, but smaller melt rates ( $<5 \text{ m a}^{-1}$ ) near the ice-shelf fronts are equally important to total meltwater production since they occur over larger areas. Integrating over the entire ice-shelf areas, we obtain basal mass budgets of  $-50 \pm 64 \text{ Gt a}^{-1}$  for Ross and  $-124 \pm 66 \text{ Gt a}^{-1}$  for Filchner-Ronne, with changes in firn air content as the largest error source.

### 1. Introduction

Increased basal melting of ice shelves has been implicated as the main driver of recent mass losses from the Antarctic Ice Sheet [Pritchard et al., 2012; Rignot et al., 2013]. Ice-shelf thinning reduces the buttressing of the adjacent grounded ice sheet, leading to accelerated flow in tributary ice streams [Dupont and Alley, 2005; Joughin et al., 2012]. Freshwater fluxes from basal melting are also important for ocean circulation and sea-ice formation around the Antarctic continent [Nicholls and Makinson, 1985; Hellmer, 2004; Bintanja et al., 2013; Rye et al., 2014]. The consequences of both effects – buttressing of land ice and freshwater production – depend not only on the net mass loss from individual ice shelves but also on the spatial and temporal distributions of basal melting. Therefore, we wish to develop accurate maps of basal mass budget that can be used to validate numerical models of ocean/ice-shelf interactions and provide benchmarks with which future ice-shelf behavior can be compared.

A common approach to obtaining local estimates of the basal mass budget of an ice shelf is to evaluate it as the residual of all other terms that contribute to the net surface elevation change [e.g., Joughin and Padman, 2003; Shepherd et al., 2003, 2004; Padman et al., 2012; Rignot et al., 2013]. This calculation is challenging because, away from the grounding zone, ice shelves are in hydrostatic equilibrium. Hence, only about 10% of the mass-related thickness changes appear in the elevation signal, while other terms including short- and long-term changes in sea level and firn air content contribute directly. Furthermore, the accuracy with which we can derive the basal component of thickness change is dependent on how well we can separate out other thickness changes that are due to surface accumulation, ice advection, and lateral spreading.

Previous studies of ice-shelf elevation changes from satellite altimetry have used either intersecting tracks (crossovers) [Shepherd et al., 2003; Zwally et al., 2005; Fricker and Padman, 2012] or near-repeat tracks [Pritchard et al., 2012] to compare elevations at fixed geographic locations; we refer to this as the “Eulerian” approach. An alternative method compares elevations in a coordinate system that moves with the ice shelf, which is akin to measuring elevation variability at snow stakes. This “Lagrangian” approach requires the ability to track the

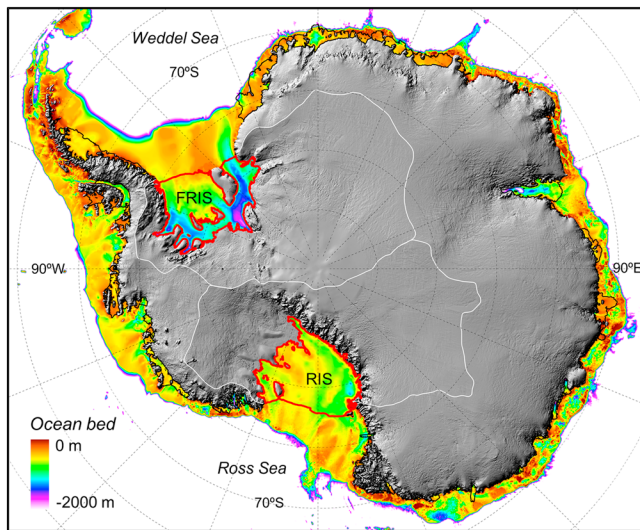


**Figure 1.** Bathymetry of the continental shelf and beneath the ice shelves surrounding Antarctica (colors) and shaded relief of the grounded ice sheet (grayscale) based on the Bedmap2 data products [Fretwell et al., 2013]. Ice shelves are outlined in red for Ross (RIS) and Filchner-Ronne (FRIS) and in black for all other ice shelves. White lines delineate the drainage basins that feed into RIS and FRIS [Zwally et al., 2012].

lateral ice motion in addition to estimating elevation changes. Dutrieux et al. [2013] derived both parameters simultaneously by matching and comparing two digital elevation models (from SPIRIT-SPOT-5 stereoscopy in 2008 [Korona et al., 2009] and airborne radar in 2011 [Vaughan et al., 2012]) over the rapidly thinning ice shelf of Pine Island Glacier. Simultaneous derivation of surface velocity and elevation changes using satellite altimetry is challenging due to the incomplete coverage of ground tracks, but two studies have demonstrated success on Ross Ice Shelf by (i) correlating surface undulations of ICESat near-repeat tracks [Marsh and Rack, 2012] and (ii) using minimum elevation difference as a criteria to find the most likely location of Lagrangian crossover points [Lee et al., 2012]. Both of these

methods have limitations; the first is limited to movement in the along-track direction, and the second is prone to errors when Lagrangian elevation changes are of comparable magnitude to surface undulations.

In this paper, we describe a Lagrangian technique for estimating ice-shelf mass budget that uses an independent velocity field obtained from radar interferometry [Rignot et al., 2011a; Scheuchl et al., 2012] to account for ice advection between time-separated altimeter measurements. We apply this technique to the two largest Antarctic ice shelves, Ross Ice Shelf (RIS) and Filchner-Ronne Ice Shelf (FRIS), located in the Ross and Weddell Sea embayments, respectively (Figure 1). These ice shelves have relatively low mean basal melt rates [Depoorter et al., 2013; Rignot et al., 2013] but produce significant net volumes of basal melt water (Tables 1 and 2) because of their large areas. We document all processes that contribute to elevation change for these two ice shelves (ocean state, firn air content, surface mass budget, and ice-flow advection and divergence) and estimate the distribution of basal mass budget as the residual of these processes.

## 2. Satellite Data

### 2.1. Surface Elevation

We used laser altimeter data from NASA's Ice, Cloud and land Elevation Satellite (ICESat) [Schutz et al., 2005]. The ICESat altimeter operated in "campaign mode" between October 2003 and October 2009, acquiring data

**Table 1.** Comparison of Mass Budget Estimates for the Ross Ice Shelf From Various Publications (Steady State Numbers in Parentheses)

Ross Ice Shelf	GLF <sup>a</sup> (Gt a <sup>-1</sup> )	IFF <sup>b</sup> (Gt a <sup>-1</sup> )	SMB <sup>c</sup> (Gt a <sup>-1</sup> )	BMB <sup>d</sup> (Gt a <sup>-1</sup> )	NMB <sup>e</sup> (Gt a <sup>-1</sup> )	Time	Method
This study	+136	-144	+66 (+69)	-50 (-61)	+7	2003–2009	Altimetry
Rignot et al. [2013]	+129	-146	(+65)	-48 (-48)	0	2003–2009	Flux/altimetry
Depoorter et al. [2013]	+120	-147	(+61)	(-34)	(0)	2007–2009	Flux
Shepherd et al. [2010]					+71	1994–2008	Altimetry
Timmermann et al. [2012]				-260			Ocean model
Kusahara and Hasumi [2013]				-103			Ocean model
Arzeno et al. [2014]				-138			Ocean model

<sup>a</sup>Grounding-line flux.

<sup>b</sup>Ice-front flux.

<sup>c</sup>Surface mass budget.

<sup>d</sup>Basal mass budget.

<sup>e</sup>Net mass budget.

**Table 2.** Comparison of Mass Budget Estimates for the Filchner-Ronne Ice Shelf From Various Publications (Steady State Numbers in Parentheses)

Filchner-Ronne Ice Shelf	GLF <sup>a</sup> (Gt a <sup>-1</sup> )	IFF <sup>b</sup> (Gt a <sup>-1</sup> )	SMB <sup>c</sup> (Gt a <sup>-1</sup> )	BMB <sup>d</sup> (Gt a <sup>-1</sup> )	NMB <sup>e</sup> (Gt a <sup>-1</sup> )	Time	Method
This study	+241	-237	+85 (+77)	-124 (-82)	-35	2003–2009	Altimetry
Rignot <i>et al.</i> [2013]	+254	-232	(+73)	-155 (-94)	-61	2003–2009	Flux/altimetry
Depoorter <i>et al.</i> [2013]	+230	-250	(+70)	(-50)	(0)	2007–2009	Flux
Jougin and Padman [2003]	+190 <sup>f</sup>	-216	(+109 <sup>f</sup> )	(-83)	(0)	2003–2009	Flux
Shepherd <i>et al.</i> [2010]					+225	1994–2008	Altimetry
Makinson <i>et al.</i> [2011]					-92		Ocean model
Hellmer <i>et al.</i> [2012]					-82		Ocean model
Timmermann <i>et al.</i> [2012]					-138		Ocean model
Kusahara and Hasumi [2013]					-176		Ocean model

<sup>a</sup>Grounding-line flux.<sup>b</sup>Ice-front flux.<sup>c</sup>Surface mass budget.<sup>d</sup>Basal mass budget.<sup>e</sup>Net mass budget.<sup>f</sup>Includes grounded ice sheet areas within flux-gate boundaries.

along the same ground tracks of a 33 day subcycle of the 91 day repeat orbit, repeated 2–3 times per year with a total of 17 campaigns. The measurements of surface elevation ( $h$ ) were separated along-track by  $\sim 170$  m and represent averages over elliptical footprints with axes of 50–100 m [Abshire *et al.*, 2005]. We used data from Release 633 of the GLA12 Antarctic and Greenland Ice Sheet Altimetry data product, which we converted from the TOPEX/Poseidon reference ellipsoid to WGS84. We applied the GLA12 saturation correction [Fricker *et al.*, 2005b] and added the Gaussian-Centroid offsets to the elevations based on the appropriate parameters in the GLA05 product [Borsa *et al.*, 2013]. We replaced the GLA12 ocean tide corrections with extracted values from the CATS2008a model, an update to the regional inverse barotropic tide model described by Padman *et al.* [2002]. We also corrected for the inverse barometer effect ( $-1$  cm/hPa) [Chelton and Enfield, 1986; Padman *et al.*, 2003], using pressure values from the GLA12 product with respect to a reference pressure of 1011.3 hPa. The mean and standard deviation of the correction was  $-0.34 \pm 0.13$  m, reflecting a generally lower air pressure around Antarctica. The efficacy of the correction was confirmed by a 4 cm decrease in the interquartile range of elevation differences at crossover points within individual campaigns.

The largest remaining elevation errors are due to multiple scattering of photons in clouds and blowing snow which delays the return pulse, causing elevation estimates that are too low [Mahesh *et al.*, 2002]. We tested various forms of parameter-based data editing to remove cloud-affected data [Smith *et al.*, 2009] by analyzing the resulting root-mean-square (RMS) elevation difference at crossover points within individual campaigns. We found that the RMS error was most sensitive to the GLA12 IceSvar parameter that describes the misfit between the return waveform and the default Gaussian model that was fit to the return waveform to estimate surface elevation. The RMS error converged to about 0.25 m after removing the data with the 5% highest waveform misfits in each campaign, so we adopted that as a data-editing threshold, retaining 95% of the original data.

## 2.2. Surface Velocity

We used published Antarctic ice velocity maps derived from interferometry and feature-tracking of synthetic aperture radar (SAR) data obtained through the IPY-MEaSUREs program [Rignot *et al.*, 2011a; Scheuchl *et al.*, 2012]. The RIS velocities (Figure 2a) were based on RADARSAT-2 SAR scenes from 2009 [Scheuchl *et al.*, 2012], whereas the FRIS velocities (Figure 2c) were compiled from different SAR data, predominantly acquired in 2007–2009 [Rignot *et al.*, 2011a]. Both products have a spatial resolution of 900 m in the polar stereographic projection. Since these velocities were derived from satellite passes separated by short periods (typically  $< 50$  days), we validated their longer-term consistency with multiyear velocities from repeat MODIS imagery during 2001–2009 [Haug *et al.*, 2010]. Based on this independent data set and a comparison with another velocity field from 1997 [Scheuchl *et al.*, 2012], we estimated a local velocity uncertainty of  $30$  m a<sup>-1</sup> and a potential average velocity difference of up to  $10$  m a<sup>-1</sup> with respect to the ICESat period (2003–2009). The RIS velocities from 2009 are likely lower than the average value for 2003–2009 due to a decadal deceleration over most of the ice-shelf interior [Scheuchl *et al.*, 2012; Hulbe *et al.*, 2013], but the magnitude is too small ( $1\text{--}3$  m a<sup>-2</sup>) to warrant a correction over the 6 year period.

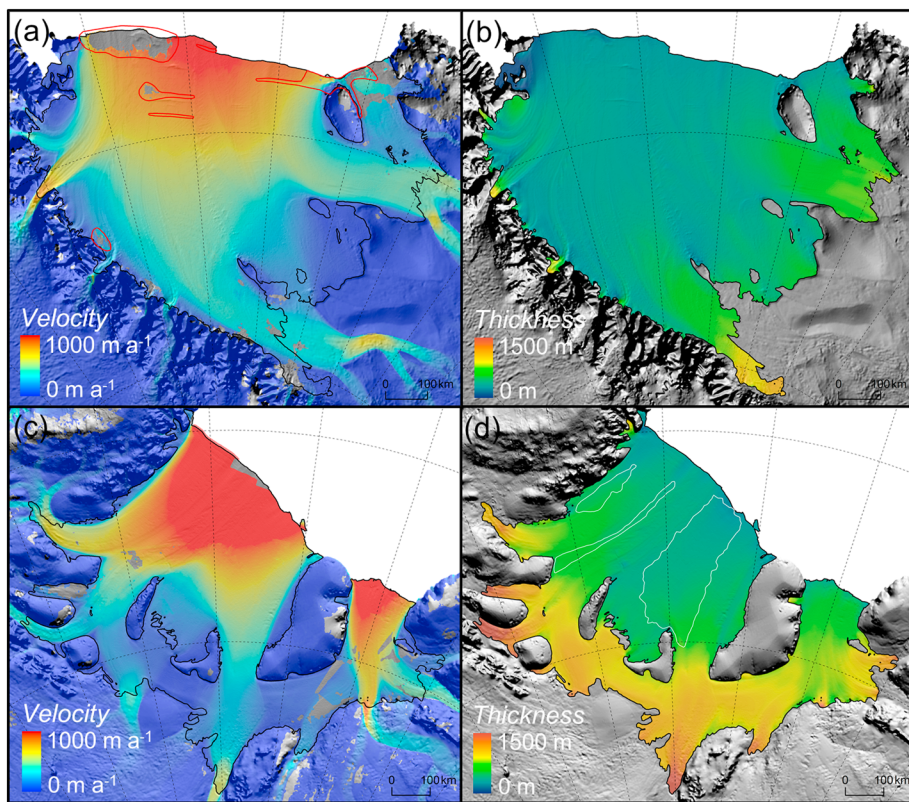


**Figure 2.** Surface velocity for (a) Ross Ice Shelf and (c) Filchner-Ronne Ice Shelf obtained from synthetic aperture radar [Rignot et al., 2011a; Scheuchl et al., 2012]. Red outlines in Figure 2a show areas where surface velocities were excluded due to expanding ice shelf rifts or spurious velocity data. (b and d) Ice thickness estimates from a firn density model [Ligtenberg et al., 2011] and ICESat altimetry. White outlines in Figure 1d indicate areas where the estimated depth-fraction of marine ice is higher than 25% [Lambrecht et al., 2007]. Background image is a shaded relief of the surface topography.

### 2.3. Ice Shelf Extent and Thickness

We generated an ice-shelf mask by combining existing products of grounding lines and coastlines. We started with discontinuous grounding lines from SAR interferometry [Rignot et al., 2011b] and ICESat repeat-track altimetry [Brunt et al., 2010, 2011] and then filled in gaps with the complete image-based products of MOA [Scambos et al., 2007] and ASAID [Bindschadler et al., 2011]; see Depoorter et al. [2013] for additional details. The resulting grounding line was combined with the MOA ice-shelf front locations of 2003–2004 [Scambos et al., 2007] to derive an ice-shelf mask corresponding to the start of the ICESat mission. During 2003–2009, we found that the frontal positions, identified by large jumps in the ICESat along-track elevations, advanced in accordance with the surface velocity field. This caused a ~6 km seaward expansion of both ice shelves by the end of the ICESat mission in 2009.

Ice thicknesses ( $H$ ) for RIS and FRIS have been partially measured by ice-penetrating radar and seismic measurements, but published maps of  $H$  with complete coverage rely mostly on hydrostatic inversion of ice freeboard estimates from satellite altimetry and firn density modeling [Griggs and Bamber, 2011; Depoorter et al., 2013; Fretwell et al., 2013]. All of these maps are based on densely sampled ERS-1 radar altimetry from its geodetic phases (1994–1995), up to its latitudinal limit of 81.5°S, and ICESat laser altimetry (2003–2008) south of 81.5°S. To obtain a methodically consistent field of ice thickness, we generated our own maps (Figures 2b and 2d) from ICESat-derived freeboard heights that we corrected for the mean dynamic topography of the ocean [Andersen et al., 2013] and the firn air content derived from a semiempirical firn densification model [Ligtenberg et al., 2011]. The assumption of hydrostatic equilibrium breaks down in the flexure zone near the ice-shelf grounding line, but this is typically limited to the landward 1–8 km of the ice shelves [Brunt et al., 2010, 2011]. More details about the thickness calculations and uncertainties can be found in the supporting information.

### 3. Eulerian Versus Lagrangian Elevation Changes

#### 3.1. Components of Elevation Change

We investigate both Eulerian and Lagrangian rates of change of ice-shelf surface elevation ( $h$ ); we denote these by  $\partial h / \partial t$  and  $Dh / Dt$ , respectively. Eulerian  $\partial h / \partial t$  on ice shelves can be described by the following equation [Shepherd *et al.*, 2003, 2004]:

$$\frac{\partial h}{\partial t} = \frac{\partial h_w}{\partial t} - M \frac{\partial}{\partial t} \left( \frac{1}{\rho_w} \right) + \frac{\partial H_a}{\partial t} + \left( \frac{1}{\rho_i} - \frac{1}{\rho_w} \right) (\dot{M}_s + \dot{M}_b + M \nabla \cdot v + v \cdot \nabla M) \quad (1)$$

where  $h_w$  is sea level height (m),  $H_a$  is the firn air content (m),  $M$  is the ice-shelf mass per unit area ( $\text{kg m}^{-2}$ ),  $\rho_w$  and  $\rho_i$  are densities of ocean water and meteoric ice ( $\text{kg m}^{-3}$ ),  $M_s$  and  $M_b$  are rates ( $\partial / \partial t$ ) of surface and basal mass change ( $\text{kg m}^{-2} \text{s}^{-1}$ ), and  $v$  is horizontal surface velocity ( $\text{m s}^{-1}$ ). The terms on the right side of the equation are elevation changes due to (1) sea level variations including ocean tides and dynamic topography, (2) ocean density changes under free-floating ice, (3) changes in firn air content, (4) surface mass budget, (5) basal mass budget, (6) ice flow divergence, and (7) advection of ice thickness gradients.

If the reference frame advects with the ice-shelf flow ( $v$ ) in a Lagrangian sense, the last term of equation (1) vanishes and we obtain the equation for Lagrangian  $Dh / Dt$ :

$$\frac{Dh}{Dt} = \frac{\partial h_w}{\partial t} - M \frac{\partial}{\partial t} \left( \frac{1}{\rho_w} \right) + \frac{\partial H_a}{\partial t} \left( \frac{1}{\rho_i} - \frac{1}{\rho_w} \right) (\dot{M}_s + \dot{M}_b + M \nabla \cdot v) \quad (2)$$

The relation between  $Dh / Dt$  and  $\partial h / \partial t$  is given by

$$\frac{Dh}{Dt} = \frac{\partial h}{\partial t} - \left( \frac{1}{\rho_i} - \frac{1}{\rho_w} \right) v \cdot \nabla M \quad (3)$$

where the latter term is the elevation signal of advection of ice thickness gradients for an ice shelf in hydrostatic equilibrium. This advection term is typically positive (ice thins downstream) and, at larger scales, it approximately compensates for the generally negative ice flow divergence caused by gravitational spreading. The sum of these dynamic thickness changes equals the net ice flux through a fixed ice shelf perimeter, which we here refer to as the “dynamic mass budget.”

#### 3.2. Calculation of Elevation Change From ICESat Altimetry

For the Eulerian approach, we used a “nearest-neighbor” technique where  $\partial h / \partial t$  is estimated from the elevation difference between two ICESat footprints acquired in different campaigns with a maximum center-point separation of 100 m. This is similar to the “overlapping-footprint” approach of Gunter *et al.* [2013] and Hofton *et al.* [2013] except that our maximum separation is about twice the value that they adopted so that we obtain more pairs of data points. We justify our larger value based on the relatively flat ice-shelf surfaces. With this criterion, typically about 50% of the data in any pair of campaigns can be used. We estimated long-term  $\partial h / \partial t$  for all footprint pairs separated in time by at least 3 years and acquired during the same season, either October–December or February–April. To generate time series, we also estimated short-term  $\partial h / \partial t$  between consecutive campaigns regardless of season. For both the long-term and short-term cases, we averaged the individual  $\partial h / \partial t$  estimates within nonoverlapping clusters of 5 km radius along the tracks while using a 3-sigma edit to remove outliers. We then gridded the averaged  $\partial h / \partial t$  clusters to the same grid as the velocity data by ordinary kriging with a spherical semivariogram model.

For the Lagrangian approach, we first translated the footprints according to the SAR-based velocity field and the time interval between observations and then applied a similar “nearest-neighbor” technique to the translated data. Our processing consisted of four steps. (i) We extracted two-dimensional surface velocities at the locations of all ICESat footprints in a selected campaign using bilinear interpolation. (ii) We translated the campaign footprints to the epochs of other campaigns by multiplying the velocities by the average time difference between the campaigns. This was done at monthly time steps and new velocities were extracted at each step. (iii) Working with pairs of ICESat campaigns, we estimated  $Dh / Dt$  from the elevation difference between a translated footprint and its nearest neighbor from the other campaign. The calculations were done both forward and backward in time to reduce potential biases from ice acceleration along flow paths. (iv) After repeating the preceding steps for all relevant combinations of campaigns, the values of  $Dh / Dt$  were edited, averaged, and gridded as for the Eulerian approach.

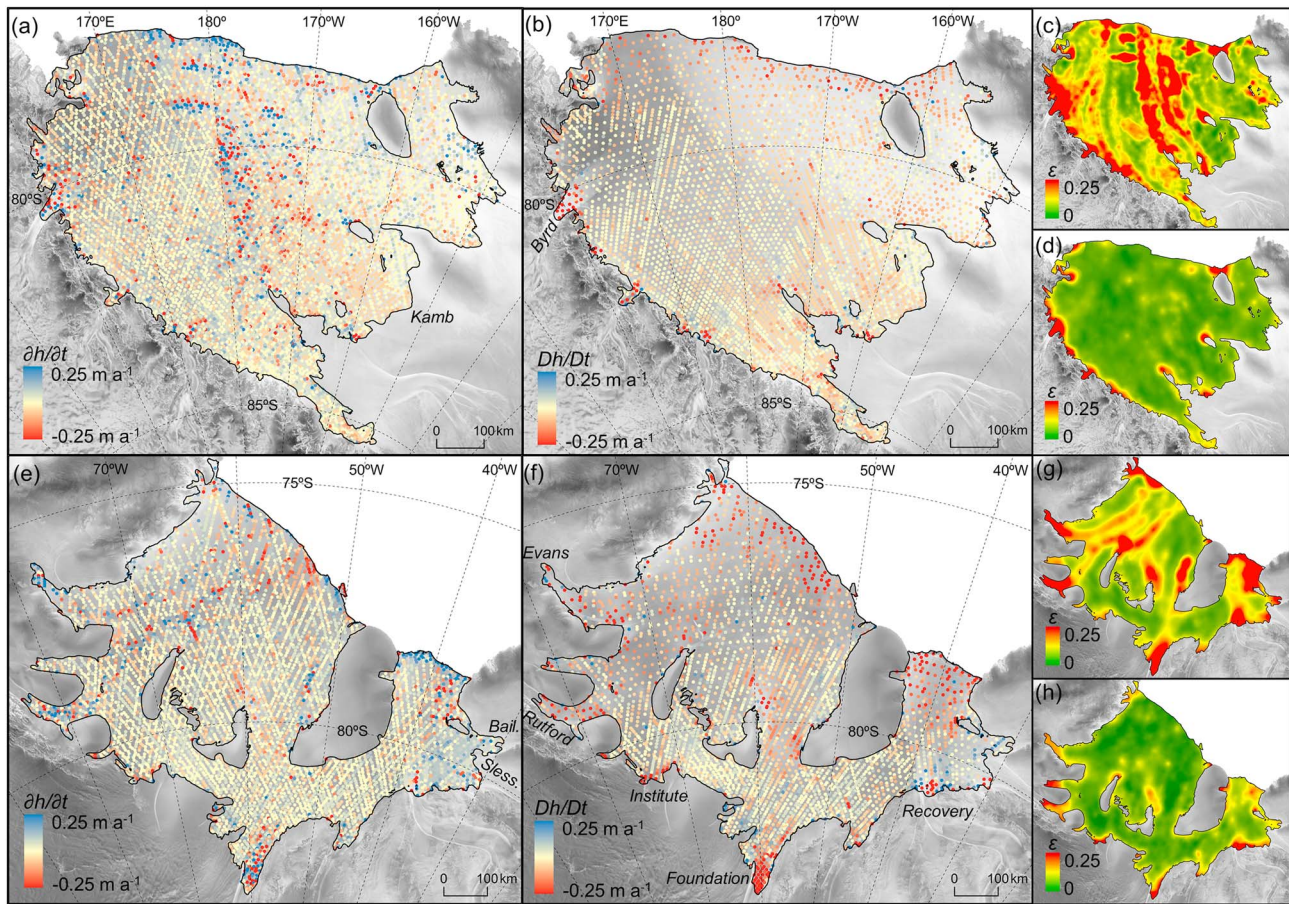


**Figure 3.** Eulerian elevation rates ( $\partial h / \partial t$ ) between 2003 and 2009 for (a) Ross Ice Shelf and (e) Filchner-Ronne Ice Shelf. (b and f) Corresponding Lagrangian elevation rates (Dh/Dt). The small panels show the associated uncertainty for (c and g)  $\partial h / \partial t$  and (d and h) Dh/Dt. Background image is the Radarsat SAR Mosaic of Antarctica (RAMP) [Jezek and RAMP Product Team, 2002].

The uncertainties of  $\partial h / \partial t$  and Dh/Dt are difficult to quantify due to a mix of random and systematic errors that are variable in time and space. We assume that random errors are contained in the local  $\partial h / \partial t$  variability within individual clusters, whereas systematic errors can be accounted for separately. For the Lagrangian approach, we estimated the local Dh/Dt uncertainty at ~5 km scales from

$$\varepsilon_{\text{Dh/Dt}} = \sqrt{\sigma_{\text{Dh/Dt}}^2 + \varepsilon_{\text{bias}}^2 + \left( \frac{\text{Dh} \varepsilon_v}{\text{Dt} v} \right)^2} \quad (4)$$

where  $\sigma_{\text{Dh/Dt}}$  is the standard deviation of Dh/Dt within each 5 km cluster,  $\varepsilon_{\text{bias}}$  is a potential erroneous elevation trend in the ICESat data due to time-dependent observational issues (assumed to be <5 mm a<sup>-1</sup>), and  $\varepsilon_v$  is the local surface velocity error (30 m a<sup>-1</sup>) as determined from the comparison with independent velocity fields from different time periods. The velocity-induced error in Dh/Dt is expected to be approximately proportional to the relative velocity uncertainty ( $\varepsilon_v/v$ ). We estimated Eulerian  $\partial h / \partial t$  uncertainties in a similar way except there is no velocity-induced error in that approach. Gridded uncertainty maps are shown in Figure 3 together with the cluster-averaged results of  $\partial h / \partial t$  and Dh/Dt.

### 3.3. Comparison of Eulerian $\partial h / \partial t$ and Lagrangian Dh/Dt

The velocity-based translation used in the Lagrangian method significantly reduces the number of valid pairs of nearby observations compared the Eulerian method. Point separation occurs most rapidly when surface velocities are high and ice flow does not align with the direction of the ICESat tracks, so that Dh/Dt calculations can often only be made at orbit crossover points, not along repeat tracks. This is a major limitation to the Lagrangian method for ice shelves at lower latitudes where the tracks are farther apart. The only ice shelves

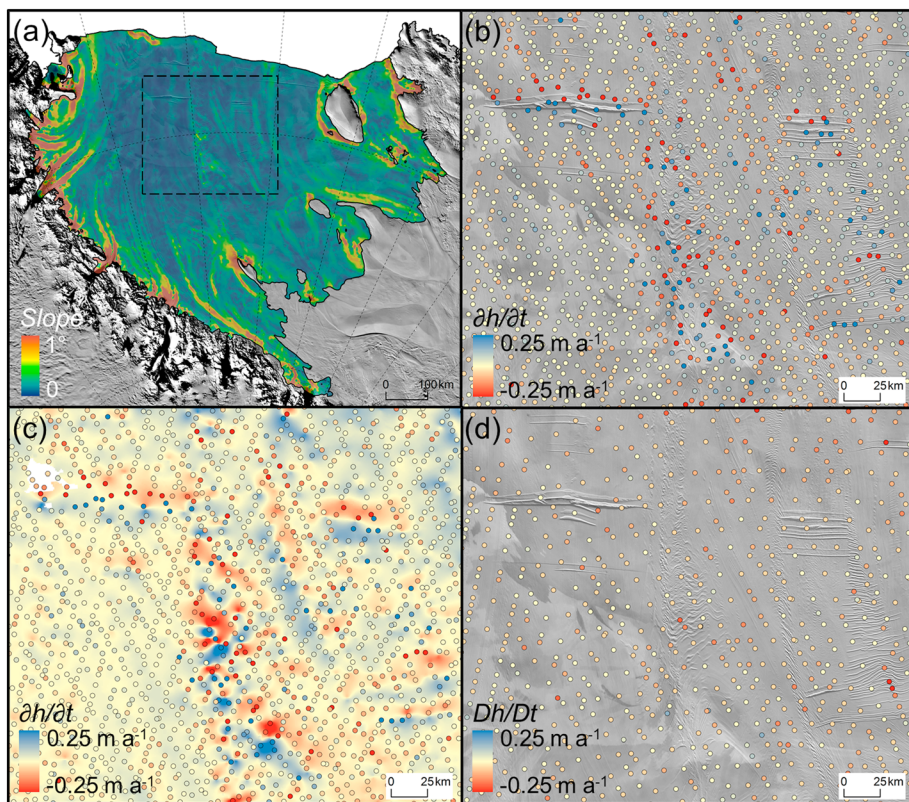


**Figure 4.** (a) Surface slopes over Ross Ice Shelf estimated from gridded ICESat elevations. Background image is the MODIS Mosaic of Antarctica (MOA) [Scambos *et al.*, 2007]. The dashed box indicates the location of the other panels which show (b and c) Eulerian  $\partial h / \partial t$  and (d) Lagrangian  $Dh / Dt$  elevation change rates, as colored dots. Background grid in Figure 4c is the estimated  $\partial h / \partial t$  from advection of surface gradients (Figure 5a), whereas the background in Figures 4b and 4d is a transparent overlay of MOA2003 (most visible) and MOA2009 (least visible), showing a northward movement (i.e., crevasses and rifts) of 3–6 km during the 2003–2009 period. The mean and standard deviation of  $\partial h / \partial t$  and  $Dh / Dt$  within the box are  $-15 \pm 230$  mm a<sup>-1</sup> and  $-47 \pm 50$  mm a<sup>-1</sup>, respectively.

where the Lagrangian technique had sufficient data coverage were the two largest ice shelves that are at higher latitude, RIS and FRIS. For RIS, the numbers of analyzed elevation changes were 3.5 million (Eulerian  $\partial h / \partial t$ ) and 0.7 million (Lagrangian  $Dh / Dt$ ), and for FRIS, the numbers were 1.9 million and 0.5 million. The average separation distance between compared neighbor points was  $\sim 64$  m for both ice shelves. Spatial averaging in 5 km clusters generated  $\sim 8300$  ( $\partial h / \partial t$ ) and  $\sim 4700$  ( $Dh / Dt$ ) estimates for RIS, and  $\sim 5900$  and  $\sim 3400$  for FRIS (Figure 3).

The Lagrangian  $Dh / Dt$  maps over RIS and FRIS show clear spatial patterns with reduced noise levels compared to the corresponding  $\partial h / \partial t$  maps (Figure 3). Lagrangian processing improved the standard deviation in the 5 km clusters from  $0.17$  to  $0.07$  m a<sup>-1</sup> for RIS and from  $0.15$  to  $0.08$  m a<sup>-1</sup> for FRIS, confirming that the method can compensate for downstream advection of surface roughness. Figure 4 illustrates this over a rough zone of RIS that contains some large rifts [Fricker *et al.*, 2005a]: most large values of  $\partial h / \partial t$  around rifts and surface undulations are a result of ice advection rather than the climatic and oceanic processes we seek to detect. Real small-scale variations in basal mass budget typically occur in the vicinity of basal channels, ridges, and crevasses/rifts that also advect with ice flow [Dutrieux *et al.*, 2013]. For these reasons, we use only the Lagrangian  $Dh / Dt$  for estimating basal mass budget in section 4.

The difference between  $\partial h / \partial t$  and  $Dh / Dt$  yields the dynamic elevation changes from the advection of hydrostatically compensated ice thickness gradients (Figure 5). These can also be estimated directly from the fields of surface velocity ( $v$ ) and mass-equivalent ice thickness ( $M$ ) according to equation (3). On the broad scale, the resulting elevation-change fields are consistent with each other, but locally (<10 km), they sometimes deviate substantially due to the different length scale of resolved variability. For example, the  $\partial h / \partial t$  and  $Dh / Dt$

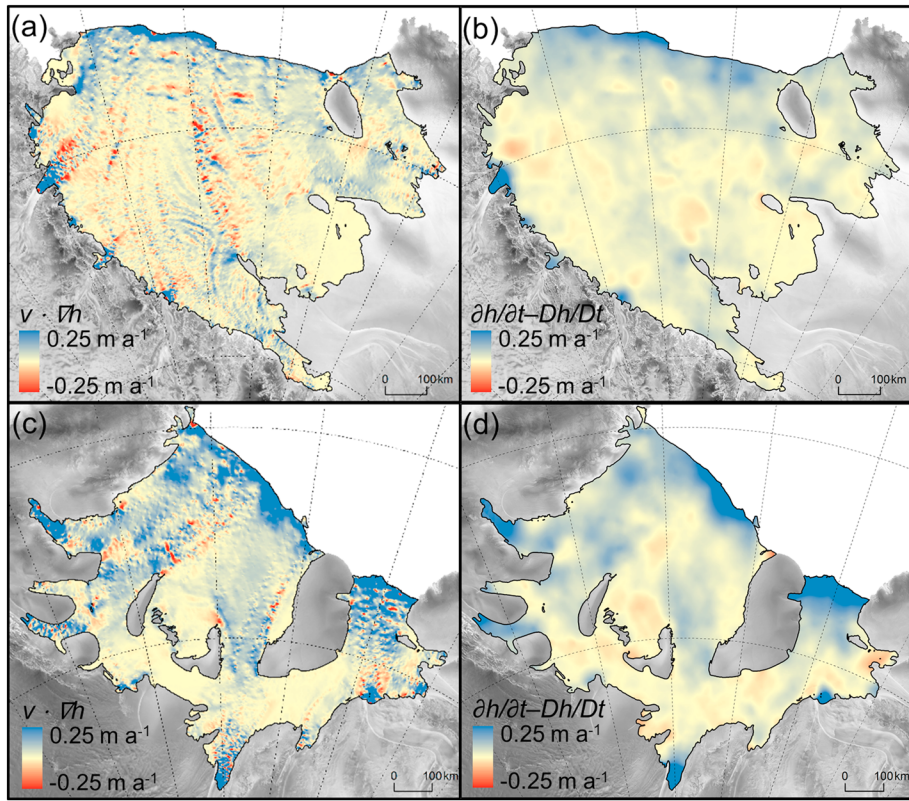


**Figure 5.** Elevation rates due to advection of surface elevation gradients on (a) Ross Ice Shelf and (c) Filchner-Ronne Ice Shelf. (b and d) Corresponding estimates from the difference between gridded Eulerian ( $\partial h / \partial t$ ) and Lagrangian ( $Dh / Dt$ ) elevation rates. Figures 5a and 5c show fine-scale advection based on neighbor grid cells whereas Figures 5b and 5d show large-scale patterns used in the mass budget calculations.

estimates resolve elevation changes within a few hundred meters distance that are then interpolated to unmeasured areas, whereas the ice thickness gradients are based on gridded fields of ICESat elevations that have been interpolated across data gaps of several kilometers. When averaged over each ice shelf, the estimates for the advection term of  $\partial h / \partial t$  via the two approaches agree within  $6 \text{ mm a}^{-1}$  and show a substantially higher elevation increase averaged over FRIS than RIS ( $81 \text{ vs. } 33 \text{ mm a}^{-1}$ ). This is also evident at shorter time scales from the difference between the area-averaged time series of Eulerian and Lagrangian elevation in Figure 6. The Eulerian–Lagrangian curves diverge at steady rates for both ice shelves, but with the rate for FRIS being more than twice the rate for RIS, mainly due to the larger ice thickness gradients of FRIS (Figure 2).

#### 4. Basal and Net Mass Budget From Lagrangian $Dh / Dt$

In the following sections, we estimate the oceanic and climatic elevation change components (4.1 and 4.2), the dynamic mass fluxes (4.3), and the basal mass budget from the residual of all other components (4.4). We also derive the net mass budget from both Lagrangian  $Dh / Dt$  and Eulerian  $\partial h / \partial t$  (4.5).

##### 4.1. Ocean Variability

Changes in sea level and ocean density under ice shelves are poorly constrained due to limited direct observations. Even north of the ice fronts, extensive sea-ice coverage around Antarctica makes it difficult to determine sea level variations from satellite altimetry. We used AVISO (Archiving, Validation, and Interpretation of Satellite Oceanographic Data) [e.g., Le Traon *et al.*, 1998] multimission Ssalto/Duacs product for 1993–2012 to extract sea-level trends ( $\partial h_w / \partial t$ ) seaward of the region covered by ice shelves and sea ice. We extrapolated these results to the RIS and FRIS fronts, obtaining mean trends of  $3.8 \text{ mm a}^{-1}$  and  $3.2 \text{ mm a}^{-1}$ , respectively. The values are close to the global average of  $3.2 \pm 0.6 \text{ mm a}^{-1}$  stated for the same product. Errors on estimates of  $\partial h_w / \partial t$  for specific regions, and for shorter time scales such as the 6 year ICESat record, will be much larger

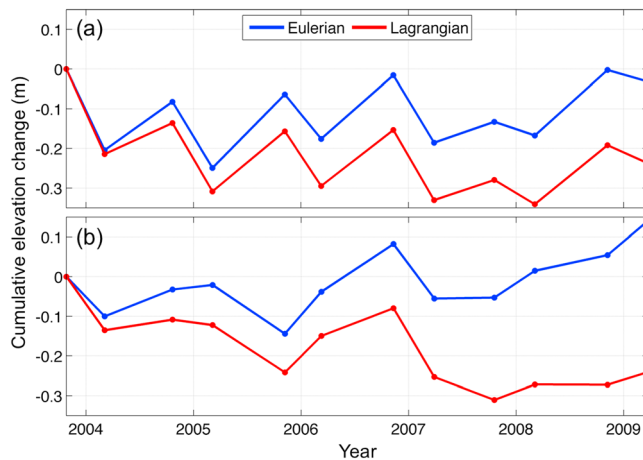


**Figure 6.** Time series of area-averaged surface elevation using the Eulerian and Lagrangian approaches for (a) Ross Ice Shelf and (b) Filchner-Ronne Ice Shelf.

(equation (2)). The shelf water in front of RIS at depths below 200 m has freshened ( $\sim 0.1$  psu) and cooled ( $\sim 0.5^\circ\text{C}$ ) between the late 1970s and 2007 [Jacobs and Giulivi, 2010]. This converts into a negative trend in potential density of  $\sim 0.005 \text{ kg m}^{-3} \text{ a}^{-1}$ , corresponding to an ice-shelf surface lowering of  $< 1 \text{ mm a}^{-1}$  for typical ice drafts of RIS. Looking at annual variations in density from depth profiles near Ross Island [Jacobs and Giulivi, 2010] and seasonal variations from a 1 year Argo float record [Roemmich and Gilson, 2009] near the Ross Sea continental shelf, we find that the variability in potential density is typically within  $0.04 \text{ kg m}^{-3}$  for the density term in equation (2). Based on these findings, we assign an equivalent surface elevation rate of  $0 \pm 2 \text{ mm a}^{-1}$ . For the average  $\rho_w$  we use a value of  $1028 \pm 1 \text{ kg m}^{-3} \text{ a}^{-1}$  as obtained from borehole observations of ocean properties at the bases of RIS [Foster, 1983] and FRIS [Nicholls et al., 1997].

#### 4.2. Surface Mass Budget and Firn Air Content

Recent altimetric studies of ice-shelf basal mass budget have relied on output from the regional climate model RACMO [Lenaerts et al., 2012] and a firn densification model [Ligtenberg et al., 2011] to separate elevation changes due to surface and basal processes [Padman et al., 2012; Rignot et al., 2013]. On broad spatial scales, modeled surface mass budget (SMB) estimates are generally consistent with field observations [Lenaerts et al., 2012]; however, local differences can be large, especially over time periods shorter than a decade. Field data also have considerable uncertainties that can lead to large errors when extrapolated to unmeasured areas and time periods. We chose an observational approach based on decadal field measurements to determine the steady state SMB, and ICESat observations over ice rises and the adjacent grounded ice sheet to estimate the SMB anomalies and changes in firn air content concurrent with the ICESat data set under the assumption that elevation changes are caused by snowfall anomalies.

We obtained historic SMB measurements from GLACIOCLIM-SAMBA, an updated and quality controlled SMB data set for Antarctica [Favier et al., 2013], and from two FRIS traverses along the extended flowlines of Rutford Ice Stream [Jenkins and Doake, 1991] and Foundation Ice Stream [Graf et al., 1999]. We selected all SMB points that spanned 9 years or longer and gridded them using kriging interpolation (supporting information) to derive long-term SMB fields for the period 1945–1995, which we take to represent steady state conditions (Figure 7). The derived spatial patterns agree well with passive-microwave satellite data [Zwally and Giovinetto, 1995; Vaughan et al., 1999] and regional climate modeling [Lenaerts et al., 2012]. Integrating the SMB fields over the ice-shelf areas, we obtain steady state SMB estimates of  $+69 \pm 10 \text{ Gt a}^{-1}$  for RIS and  $+77 \pm 11 \text{ Gt a}^{-1}$  for FRIS. This is consistent with the regional climate model RACMO2 which indicates a SMB of  $+61 \pm 17 \text{ Gt a}^{-1}$  for RIS and  $+70 \pm 20 \text{ Gt a}^{-1}$  for FRIS over the period 1979–2010 [Depoorter et al., 2013].

We investigated potential changes in firn layer thickness by analyzing elevation changes over ice rises and the grounded ice sheet around the ice-shelf perimeter. We defined a “grounded-ice perimeter zone” that includes all grounded ice within 100 km of the grounding line (Figure 7). We estimated Eulerian  $\partial h/\partial t$  for this zone using an algorithm that accounts for static surface slopes by fitting surface planes to segments of

than for the 20 year global average. Based on variability of  $\partial h_w/\partial t$  north of the sea-ice edge in the Southern Ocean, and analysis of short-term ocean processes seaward of the ice shelves in the global ocean state model ECCO-2 [Menemenlis et al., 2008], we estimate that the error contribution from sea-level change is about  $5 \text{ mm a}^{-1}$  over the ICESat period. Combining these estimates, we set the sea-level term ( $\partial h_w/\partial t$ ) in equation (2) to  $3 \pm 5 \text{ mm a}^{-1}$  for both ice shelves.

Changes in ocean density ( $\rho_w$ ) also influence mass budget estimates from surface elevation changes

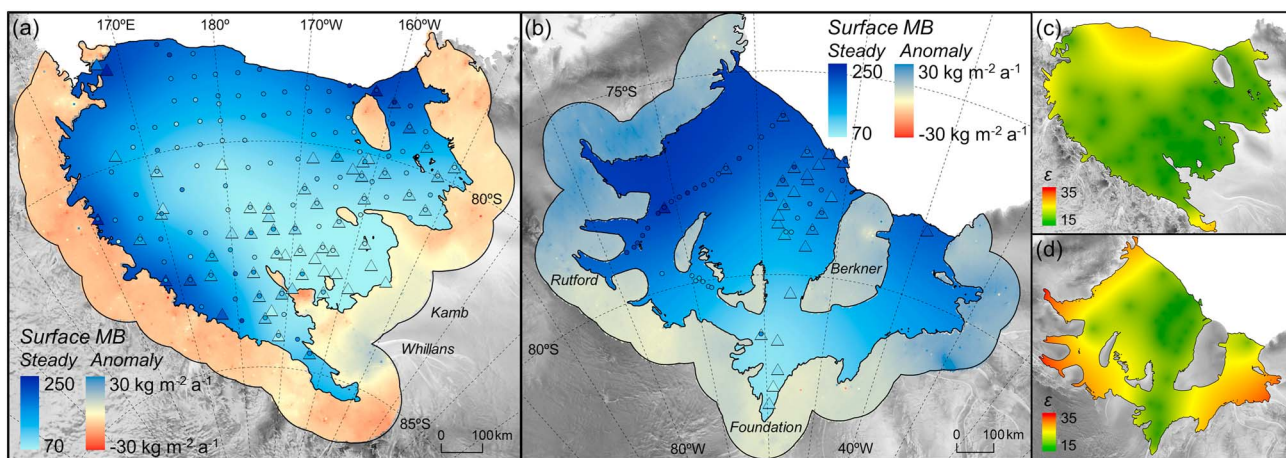


**Figure 7.** Surface mass budget (SMB) for (a) Ross Ice Shelf and (b) Filchner-Ronne Ice Shelf. The blue color scale represents estimated steady state SMB from direct measurements on the ice shelves (1945–1995), and the red-to-blue color scale represents estimated SMB anomalies in the grounded-ice perimeter zone based on large-scale elevation changes from ICESat (2003–2009). Dots indicate short-term SMB measurements (usually 1–2 years) and triangles indicate decadal measurements (9–49 years) that were used to interpolate the continuous fields of steady state SMB. (c and d) Estimated uncertainties ( $\text{kg m}^{-2} \text{a}^{-1}$ ) for the steady state SMB fields.

near repeat-track data [Smith *et al.*, 2009] and generated time series of area-averaged elevation change from the residuals of the plane fits (Figure 8). We gridded the long-term  $\partial h / \partial t$  using inverse-distance weighting to obtain large-scale spatial patterns of assumed firn thickness changes ( $\partial H_f / \partial t$ ). We then multiplied  $\partial H_f / \partial t$  by a fixed firn density ( $\rho_f = 380 \pm 40 \text{ kg m}^{-3}$ , supporting information) to derive SMB anomalies for each ice shelf (Figures 7a and 7b). The corresponding change in firn air content was estimated from

$$\frac{\partial H_a}{\partial t} = \left(1 - \frac{\rho_f}{\rho_i}\right) \frac{\partial H_f}{\partial t} \quad (5)$$

This is a simplified relation with several assumptions: (i) ice dynamics is in long-term equilibrium with climate processes, (ii) the grounded ice is climatologically similar to the nearby ice shelves, and (iii) accumulation was steady prior to the study period, i.e., no anomalous events pre-2003 lead to a response of the firn pack during 2003–2009. To test the validity of these assumptions, we performed a series of experiments with different data sources and selections (supporting information). We found that the results were relatively insensitive to the inclusion/exclusion of fast-flowing areas ( $>10 \text{ m a}^{-1}$ ), stagnant ice streams (Kamb Ice Stream on RIS), high elevations ( $>1000 \text{ m}$ ), steep slopes ( $>3^\circ$ ), and areas further away from the grounding line ( $>50 \text{ km}$ ).

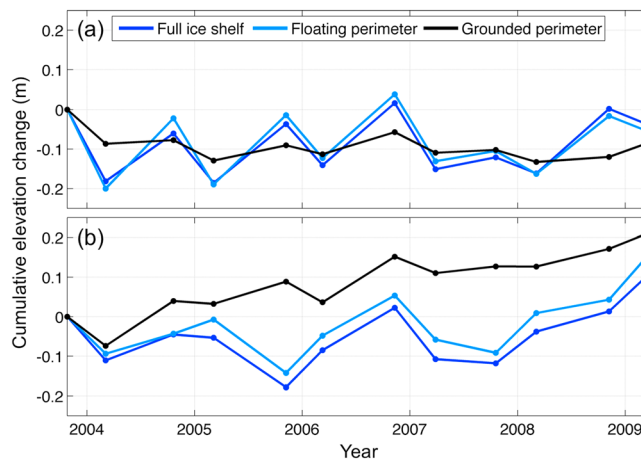


**Figure 8.** Time series of area-averaged surface elevation for the full ice shelf, the floating ice perimeter zone, and the grounded ice zone for (a) Ross Ice Shelf and (b) Filchner-Ronne Ice Shelf. See the text and Figure 7 for definitions of the perimeter zones.

We tested how representative the ice-shelf perimeter is for the ice shelf as a whole by evaluating elevation changes in a similar way for a “floating-ice perimeter zone,” defined as the seaward 50 km from the ice-shelf grounding line, and for the full ice shelf. Comparison of the resulting time series shows that, for each ice shelf, there is good agreement between the floating perimeter and the whole ice shelf (Figure 8), indicating that potential gradients in climatological anomalies have little impact on the results. We also found good correspondence between the precipitation of the grounded-ice perimeter zones and the ice shelves themselves in climate reanalysis and

**Table 3.** Area-Averaged Elevation Changes ( $Dh/Dt$ ) and Mass Budget ( $dM/dt$ ) for the Ross Ice Shelf (RIS) and the Filchner-Ronne Ice Shelf (FRIS)

Type of Ice-Shelf $Dh/Dt$	RIS $Dh/Dt$ (mm $a^{-1}$ )	FRIS $Dh/Dt$ (mm $a^{-1}$ )	RIS $dM/dt$ (kg $m^{-2} a^{-1}$ )	FRIS $dM/dt$ (kg $m^{-2} a^{-1}$ )	Data Sources
Sea level	+3 ± 5	+3 ± 5	0	0	AVISO 1993–2012
Ocean density	0 ± 2	0 ± 2	0	0	No data
Firm air content	-9 ± 10	+23 ± 10	0	0	ICESat grounded
Eulerian <sup>a</sup>	+1 ± 12	+10 ± 11	+63 ± 147	-137 ± 138	ICESat ice shelf
Lagrangian <sup>a</sup>	-38 ± 7	-65 ± 8	-269 ± 121	-769 ± 125	ICESat ice shelf
Advection <sup>b</sup>	+33 ± 5	+81 ± 7	+283 ± 38	+688 ± 55	Mass and velocities
Divergence	-35 ± 5	-80 ± 9	-299 ± 38	-678 ± 81	Mass and velocities
SMB <sup>c</sup> steady state	+16 ± 2	+21 ± 3	+139 ± 21	+176 ± 25	Field observations
SMB <sup>c</sup> anomaly	-1 ± 1	+2 ± 1	-6 ± 6	+17 ± 6	ICESat grounded
Basal mass budget	-12 ± 15	-33 ± 18	-101 ± 128	-283 ± 151	From equation (8)

<sup>a</sup> $dM/dt$  is derived from  $Dh/Dt$  after correcting for sea level, ocean density and firm air content.

<sup>b</sup>Should theoretically be similar to Eulerian minus Lagrangian (equation (3)).

<sup>c</sup>Surface mass budget.

models. However, these climate products might not be fully able to separate these zones due to the models' relatively coarse resolution (tens of km).

These analyses improve our confidence in applying the inferred SMB anomalies and firn air rates from the grounded-ice perimeter zones to the whole ice shelves as area-averaged rates with no spatial variation (Table 3). The estimated change rates are generally negative around RIS except over Kamb and Whillans ice streams (Figure 7a) where the signal is likely dominated by dynamic ice thickening [Smith *et al.*, 2005]. The elevation-change time series of the grounded zone indicates a slightly negative elevation trend with a weak seasonal cycle (Figure 8a). This is in contrast to FRIS where the grounded zone has a positive elevation trend along the entire perimeter, although there is some spatial variability (Figure 7b). The area-averaged time series shows a clear positive trend that is relatively consistent in time (Figure 8b).

Combining the field-based steady state SMB with the ICESat-based SMB anomalies, we obtain total SMB estimates for 2003–2009 of  $+66 \pm 11$  Gt  $a^{-1}$  for RIS and  $+85 \pm 12$  Gt  $a^{-1}$  for FRIS (Table 4), of which only the latter is significantly different from steady state SMB, with a positive anomaly of about 10%. The inferred firn air rates ( $\partial H_a/\partial t$ ) are  $-9 \pm 10$  mm  $a^{-1}$  for RIS and  $+23 \pm 10$  mm  $a^{-1}$ , both highly important corrections and uncertainties in equation (2) due to the lack of hydrostatic compensation in contrast to the elevation signal of the actual SMB (Table 3). A more thorough discussion of the data, methodology and uncertainties is in the supporting information.

#### 4.3. Dynamic Mass Budget

The last two terms of equation (1) constitute dynamic thickness changes due to ice advection of thickness gradients ( $M\nabla\cdot v$ ) and divergence of ice flow ( $v\cdot\nabla M$ ), which we collectively refer to as the dynamic mass budget of an ice shelf:

$$\nabla \cdot (Mv) = v \cdot \nabla M + M \nabla \cdot v \quad (6)$$

**Table 4.** Mass Budget (MB) Components for the Ross Ice Shelf (RIS) and the Filchner-Ronne Ice Shelf (FRIS) for the ICESat Period (2003–2009)

Mass Budget Component	RIS MB (Gt $a^{-1}$ )	FRIS MB (Gt $a^{-1}$ )	RIS $dM/dt$ (kg $m^{-2} a^{-1}$ )	FRIS $dM/dt$ (kg $m^{-2} a^{-1}$ )
Grounding line flux	+136 ± 27	+241 ± 43		
Ice-front flux (calving proxy)	-144 ± 12	-237 ± 15		
Dynamic mass budget	-8 ± 27	+4 ± 43	-16 ± 54	+10 ± 98
Surface accumulation	+66 ± 11	+85 ± 12	+133 ± 22	+193 ± 26
Basal accumulation	+34 ± 31	+77 ± 25	+69 ± 62	+176 ± 57
Basal ablation	-84 ± 33	-201 ± 41	-170 ± 66	-460 ± 94
Basal mass budget	-50 ± 64	-124 ± 66	-101 ± 128	-283 ± 151
Net mass budget (Lagrangian)	+7 ± 63	-35 ± 60	+14 ± 127	-81 ± 137
Net mass budget (Eulerian)	+31 ± 73	-60 ± 61	+63 ± 147	-137 ± 138

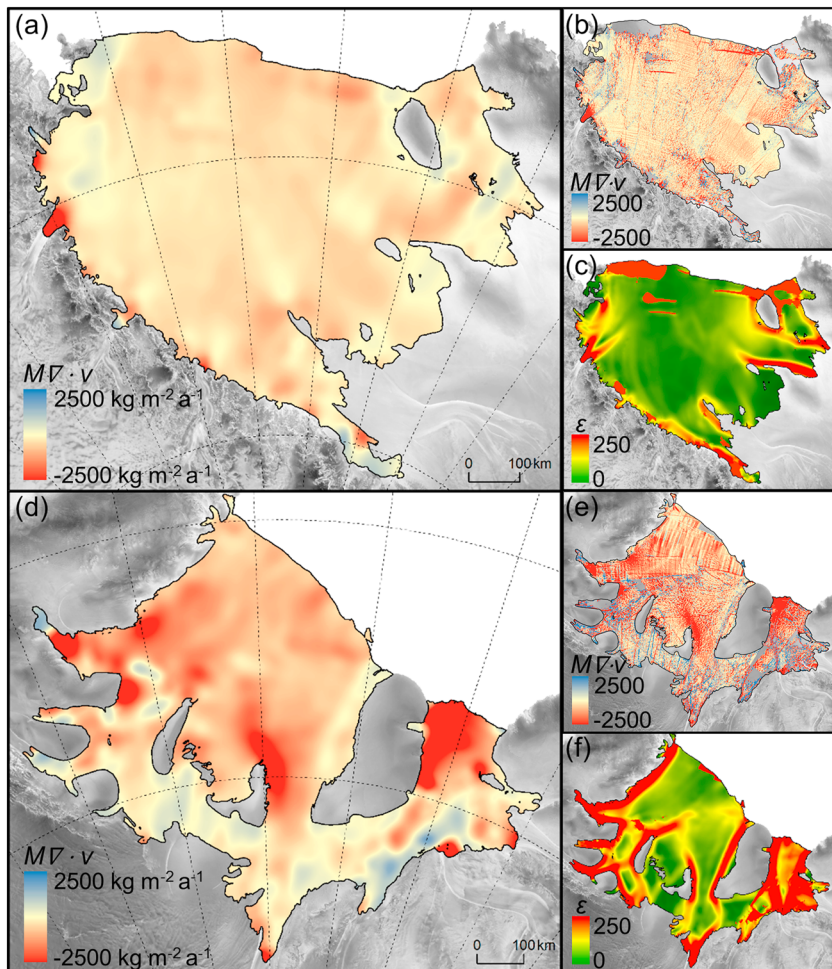


**Figure 9.** Vertical mass rates due to ice flow divergence for (a) Ross Ice Shelf and (d) Filchner-Ronne Ice Shelf, smoothed over 27 km. (b and e) Corresponding mass rates if divergence is calculated between neighboring cells without any smoothing. (c and f) Associated uncertainties ( $\text{kg m}^{-2} \text{a}^{-1}$ ) with the same units.

If we integrate the dynamic mass budget over a fixed ice-shelf area ( $A$ ), it should equal the net ice-flux ( $Q$ ) through the fixed perimeter of  $A$ :

$$Q_{\text{GL}} + Q_{\text{IF}} = \int_A \nabla \cdot (Mv) dA \quad (7)$$

where  $Q_{\text{GL}}$  is the incoming mass flux (positive) over the grounding line and  $Q_{\text{IF}}$  is the outgoing mass flux (negative) through the ice-shelf front defined at a fixed location. Only the divergence term ( $M\nabla \cdot v$ ) plays a direct role in Lagrangian elevation changes (equation (2)), but we also estimate ice advection ( $v \cdot \nabla M$ ) and frontal ice flux ( $Q_{\text{IF}}$ ) to check the consistency of our results with respect to Eulerian-derived mass budgets and external ice-flux estimates. We infer the grounding line flux ( $Q_{\text{GL}}$ ) from the residual of the three other terms but do not make a direct estimate because the lack of hydrostatic balance prevents us from deriving accurate ice thicknesses at the grounding line.

Ice-flow divergence is the horizontal stretching and compression of the ice shelf, often referred to as ice-shelf spreading [van der Veen, 1986] because unconfined flow results in ice-shelf thinning. It contributes to both Eulerian  $\partial h / \partial t$  (equation (1)) and Lagrangian  $Dh / Dt$  (equation (2)) and must be accounted for in any spatial mapping of basal mass budget. We estimated the relevant thickness changes (Figure 9) from the product of the mass-equivalent ice thicknesses and the divergence of the velocity field in the  $x$ - $y$  directions ( $M\nabla \cdot v$ ). We used a moving  $27 \times 27$  km window and fitted least-squares gradients in both directions (Figure 9). The need for such a large smoothing window is demonstrated in Figures 9b and 9e, which show the inferred mass

divergence when calculated on a cell-by-cell basis from the raw velocity and ice thickness grids. Striping is apparent at smoothing scales up to 50 km and is due to a combination of image mosaicking, satellite track orientation, ionospheric perturbations, and other SAR-related issues (B. Scheuchl, personal communication, 2014). To reduce striping, we applied a low-pass mean filter before and after the divergence calculations. We also added constraints that the filtering and divergence calculations were not allowed to extend across velocity data gaps and expanding ice shelf rifts that we masked out (Figure 2). Although rifts are sometimes associated with localized basal melting and freezing [Khazendar and Jenkins, 2003], we are unable to reliably detect such small-scale effects with our data. After the divergence calculations, we therefore filled all data gaps and masked areas by inverse-distance weighting from the edges of the data coverage. The results show that the vertical mass changes from ice flow divergence are much smaller and more homogeneous over RIS than over FRIS (Figure 9), with respective means and standard deviations of  $-299 \pm 38 \text{ kg m}^{-2} \text{ a}^{-1}$  and  $-678 \pm 81 \text{ kg m}^{-2} \text{ a}^{-1}$  (Table 3). Uncertainties are caused by a combination of ice thickness errors, mainly due to the firn air correction, and semirandom errors from the divergence calculation and its limited spatial resolution (Figures 9c and 9f).

Advection of ice thickness gradients causes a general Eulerian thickening, but with large local variations due to surface roughness. When hydrostatically compensated, it represents the difference between Eulerian and Lagrangian elevation changes, as discussed in section 3 (equation (3) and Figures 4 and 5). Here, we describe the estimation of advection-induced thickness changes from the velocity and thickness data ( $v \cdot \nabla M$ ). We estimated thickness gradients on length scales of 27 km (similar to the ice-flow divergence calculations) and multiplied these by the spatially varying velocity. No additional smoothing was needed because the thickness field is already based on kilometer-scale interpolation between ICESat tracks (supporting information). The mean and standard deviation of the resulting thickness changes are  $283 \pm 38 \text{ kg m}^{-2} \text{ a}^{-1}$  for RIS and  $688 \pm 55 \text{ kg m}^{-2} \text{ a}^{-1}$  for FRIS, which roughly balance the thinning from ice-flow divergence (Table 3). However, differences can be locally large; for example, compare the spatial patterns of thickness advection in Figures 5a and 5c with those of ice-flow divergence in Figures 9a and 9d.

Combining the advection and divergence terms as in equation (6) and integrating over the ice-shelf areas, we obtain dynamic mass budgets of  $-8 \pm 27 \text{ Gt a}^{-1}$  for RIS and  $+4 \pm 43 \text{ Gt a}^{-1}$  for FRIS (Table 4). This should equal the sum of the ice-fluxes at the grounding lines ( $Q_{GL}$ ) and the ice-shelf fronts ( $Q_{IF}$ ) at fixed locations (equation (7)). The latter is often considered as a proxy for the long-term calving flux, assuming that the ice front just fluctuates between certain boundaries. Iceberg calving on RIS and FRIS occur sporadically at multidecadal time scales [Jacobs *et al.*, 1986, 1992]. The last major calving events were from RIS in 2000 and 2002 [Martin *et al.*, 2007] and from FRIS in 1998 and 2000 [Lazzara *et al.*, 2008]. Other frontal ablation may occur but the magnitude is likely small since, during the ICESat period, the ice fronts advance at the SAR-derived velocities. We can thus estimate  $Q_{IF}$  by multiplying the gained area at the front with the corresponding average ice thickness. From the velocity field, we estimate area gains of  $610 \text{ km}^2 \text{ a}^{-1}$  for RIS and  $800 \text{ km}^2 \text{ a}^{-1}$  for FRIS. Considering mean ice-front thicknesses of 256 m (RIS) and 322 m (FRIS) ice equivalent, we obtain  $Q_{IF}$  estimates of  $-144 \pm 27 \text{ Gt a}^{-1}$  and  $-237 \pm 43 \text{ Gt a}^{-1}$ , respectively. Using these values for  $Q_{IF}$ , we can then estimate  $Q_{GL}$  from equation (7), obtaining grounding line fluxes of  $+136 \pm 27 \text{ Gt a}^{-1}$  for RIS and  $+241 \pm 43 \text{ Gt a}^{-1}$  for FRIS. All ice fluxes are consistent with previous studies that used velocities and thicknesses at the grounding line (Tables 1 and 2).

#### 4.4. Basal Mass Budget

Having estimated all other contributing processes to Lagrangian  $Dh/Dt$ , the basal mass budget (Figure 10) is obtained from the residual by rearranging equation (2):

$$\dot{M}_b = \left( \frac{1}{\rho_i} - \frac{1}{\rho_w} \right)^{-1} \left( \frac{Dh}{Dt} - \frac{\partial h_w}{\partial t} + M \frac{\partial}{\partial t} \left( \frac{1}{\rho_w} \right) - \frac{\partial H_a}{\partial t} \right) - \dot{M}_s - M \nabla \cdot v \quad (8)$$

We estimated uncertainties from the root-sum-squares of each term in equation (8) (Figures 10c and 10d), obtaining area-integrated basal mass budgets of  $-50 \pm 64 \text{ Gt a}^{-1}$  for RIS and  $-124 \pm 66 \text{ Gt a}^{-1}$  for FRIS (Table 4). The corresponding Eulerian estimates can be obtained by a similar rearrangement of equation (1) as done for Wilkins Ice Shelf by Padman *et al.* [2012], resulting in basal mass budgets of  $-26 \pm 78 \text{ Gt a}^{-1}$  and  $-149 \pm 75 \text{ Gt a}^{-1}$ . The slight difference between the two approaches arises from the treatment of ice advection ( $v \cdot \nabla M$ ) which is implicitly removed in the Lagrangian elevation changes and explicitly removed in the Eulerian approach. That also explains the slightly higher uncertainties associated with the Eulerian estimates.

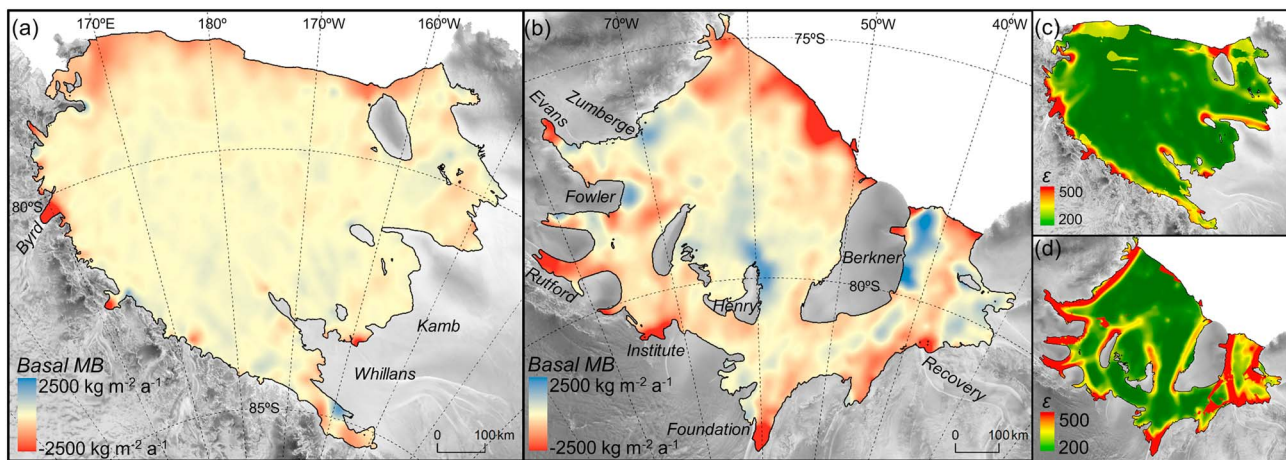


**Figure 10.** Estimated basal mass budget for (a) Ross Ice Shelf and (b) Filchner-Ronne Ice Shelf. (c and d) Associated uncertainties ( $\text{kg m}^{-2} \text{ a}^{-1}$ ).

#### 4.5. Net Mass Budget

The principal advantage of the Lagrangian method over the Eulerian method is in its ability to reduce noise in elevation change estimates and to simplify the process of deriving the basal mass budget. A disadvantage is that it is more complicated to derive the net mass budget from Lagrangian results. For Eulerian  $\partial h/\partial t$ , the net mass budget is the sum of all mass fluxes on the right side of equation (1), after accounting for all other sources of elevation change. For Lagrangian  $Dh/Dt$ , the ice advection component ( $v \cdot \nabla M$ ) must be added back to compensate for the implicit removal of this mass flux in the elevation-change processing as follows from equation (3). If we combine equations (1) and (3), the Lagrangian-based net mass budget can be derived from

$$\dot{M} = \left( \frac{1}{\rho_i} - \frac{1}{\rho_w} \right)^{-1} \left( \frac{Dh}{Dt} - \frac{\partial h_w}{\partial t} - M \frac{\partial}{\partial t} \left( \frac{1}{\rho_w} \right) + \frac{\partial H_a}{\partial t} \right) + v \cdot \nabla M \quad (9)$$

For the Lagrangian approach we obtain net mass budgets of  $+7 \pm 63 \text{ Gt a}^{-1}$  for RIS and  $-35 \pm 60 \text{ Gt a}^{-1}$  for FRIS, which is consistent with the Eulerian approach to within  $25 \text{ Gt a}^{-1}$  for both ice shelves (Table 4). Spatial patterns of net mass budget can be inferred from the Eulerian  $\partial h/\partial t$  in Figures 3a and 3e.

### 5. Discussion

#### 5.1. Interpretations of Eulerian $\partial h/\partial t$ and Lagrangian $Dh/Dt$

The Eulerian  $\partial h/\partial t$  results show that most areas of RIS and FRIS are in near steady state, with surface and basal changes being balanced by ice dynamics (Figures 3a, 3e, and 6). Local  $\partial h/\partial t$  variations are dominated by advection of surface roughness (Figure 4), making it difficult to detect larger-scale variability in mass budget. On RIS, a weak pattern of surface lowering ( $20\text{--}30 \text{ mm a}^{-1}$  on average) downstream of Kamb Ice Stream ( $84^\circ\text{S}, 165^\circ\text{W}$ ; Figure 3a) is consistent with previous analyses [Pritchard et al., 2012] and the modeled response to the stagnation of Kamb about 160 years ago [Hulbe et al., 2013]. On FRIS, the surface elevation in the embayment in front of Bailey Ice Stream and Slessor Glacier ( $80^\circ\text{S}, 35^\circ\text{W}$ ; Figure 3e) has increased at rates similar to those of the adjacent grounded ice sheet ( $60\text{--}70 \text{ mm a}^{-1}$  on average, Figures 3e and 7b). This cannot be explained solely by increased snowfall since the associated mass gain would result in an elevation change that would be hydrostatically compensated on the ice shelf but not on the grounded ice. Part of the signal could be related to a slight ice-flow deceleration that has been observed between 1997 and 2009 [Scheuchl et al., 2012].

The spatial patterns observed in the Eulerian  $\partial h/\partial t$  maps are also visible in the Lagrangian  $Dh/Dt$  maps (Figures 3b and 3f) although they are masked by an overall surface lowering (Figure 6), predominantly due to ice-flow divergence (Table 3). For the Lagrangian  $Dh/Dt$ , the impact of basal melting is expressed through strong surface lowering near the grounding zones of major ice streams including Byrd Ice Stream on RIS, and Evans, Rutford, Institute, Foundation and Recovery ice streams on FRIS. Also, there is a general increase in surface lowering towards the ice-shelf fronts of both RIS and FRIS, which has been previously

attributed to basal melting for RIS [Horgan *et al.*, 2011]. Basal freezing cannot easily be inferred from Lagrangian  $Dh/Dt$  because it often offsets dynamic thinning (Figure 10b versus Figure 9d), due to the buoyant flow of supercooled meltwater toward the shallower ice drafts where frazil accretion is more likely due to a higher pressure freezing point.

The Lagrangian technique only worked well for the RIS and FRIS where the track sampling is sufficiently dense. For ice shelves at lower latitudes than RIS and FRIS, a denser track-coverage will be needed to obtain sufficient samples of Lagrangian  $Dh/Dt$  to provide comparable error statistics. This can likely be achieved with new satellite altimeters like CryoSat-2 [Wingham *et al.*, 2006] and ICESat-2 [Abdalati *et al.*, 2010]. Orbit configurations aimed at maximizing the ground coverage, instead of frequent sampling along fewer repeat tracks, provide better estimates of Lagrangian  $Dh/Dt$ .

### 5.2. Mass Budgets and Comparison With Other Studies

Combining the Lagrangian  $Dh/Dt$  with separate estimates for ice advection, we derive net mass budgets of  $+7 \pm 63 \text{ Gt a}^{-1}$  for RIS and  $-35 \pm 60 \text{ Gt a}^{-1}$  for FRIS for 2003–2009. This is consistent with another ICESat-based Eulerian study [Rignot *et al.*, 2013] in which firn-change corrections were made from a densification model driven by a regional climate model [Pritchard *et al.*, 2012]. Two independent studies using satellite radar altimetry (ERS-1/2 and Envisat) estimated RIS and FRIS net mass budgets of  $-36 \text{ Gt a}^{-1}$  and  $+71 \text{ Gt a}^{-1}$  for the period 1992–2002 [Zwally *et al.*, 2005] and  $+71 \text{ Gt a}^{-1}$  and  $+225 \text{ Gt a}^{-1}$  for 1994–2008 [Shepherd *et al.*, 2010]. The relatively large difference between published estimates (Tables 1 and 2) cannot be entirely explained by natural variability in ice-shelf environments. For example in the case of FRIS, the two ICESat studies (our study, and Rignot *et al.* [2013]) both made corrections for a positive anomaly in firn thickness, whereas the two radar altimetry studies both made corrections for a negative anomaly [Zwally *et al.*, 2005; Helsen *et al.*, 2008]. For these climatic corrections to be valid, it would imply that the apparent negative shift in net mass budget between the radar-based estimates of the 1990s and the laser-based estimates of the 2000s has been accompanied by an even larger negative shift in the basal (and/or dynamic) mass budget of FRIS. A decadal shift in basal mass budget of this magnitude ( $>100 \text{ Gt a}^{-1}$  additional mass loss) is unlikely given that both the radar and laser studies found a slight elevation increase over their time periods. We surmise that uncertainties in observations and models have been larger than the actual variability in mass budget for RIS and FRIS.

We estimated basal mass budgets for 2003–2009 for each ice shelf from the Lagrangian-derived  $Dh/Dt$ :  $-50 \pm 64 \text{ Gt a}^{-1}$  for RIS and  $-124 \pm 66 \text{ Gt a}^{-1}$  for FRIS. These numbers are consistent (to within  $30 \text{ Gt a}^{-1}$ ) with Rignot *et al.* [2013], who used Eulerian ICESat results in combination with surface mass budget modeling and measured ice fluxes at grounding lines and the ice-shelf fronts. Without considering altimetry data, the ice-flux approach has previously been used to assess the basal mass budget required to maintain steady state conditions (i.e.,  $\partial h/\partial t = 0$ ). These estimates—for both RIS and FRIS [Depoorter *et al.*, 2013] and FRIS [Joughin and Padman, 2003]—are less negative than our short-term rates for 2003–2009 (Tables 1 and 2), but the differences are smaller than the uncertainties in each estimate, precluding identification of non-steady behavior at an ice-shelf wide scale.

Altimetry-based results are sensitive to changes in firn air content, and in this study, uncertainty in this term alone is equivalent to  $\sim 40 \text{ Gt a}^{-1}$  error in the basal mass budgets. Ocean observations and models can give independent estimates of basal mass budget for comparison, but existing model results show a large variation and are typically more negative than those based on satellite measurements (Tables 1 and 2). Improved observations and models of firn pack change are required to refine short-term variations in the basal mass budget of these large, relatively stable ice shelves. Experiments with airborne radar have yielded promising results for snow accumulation mapping in West Antarctica [Medley *et al.*, 2013], but annual layers are more difficult to identify in low-accumulation environments including RIS and FRIS.

By separately integrating regions of basal ablation and accumulation in Figure 10, we can estimate total amounts of basal melting and freezing for each ice shelf. For RIS, the total basal melting is  $84 \pm 33 \text{ Gt a}^{-1}$  and the compensating freezing is  $34 \pm 31 \text{ Gt a}^{-1}$  (Table 4). The mass turnover rates on FRIS are about twice as large, with  $201 \pm 41 \text{ Gt a}^{-1}$  of melting and  $77 \pm 25 \text{ Gt a}^{-1}$  of freezing. These numbers are slightly higher than a previous steady state estimate for parts of FRIS based on volume-flux divergence [Joughin and Padman, 2003], but the difference is not statistically significant.

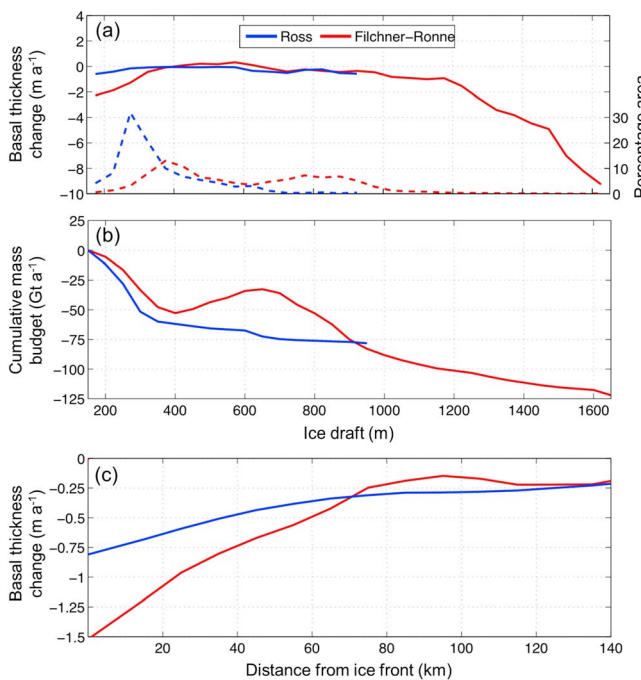


**Figure 11.** (a) Basal ice thickness change (<0 implies melting) averaged in 50 m bins of ice draft. Dashed lines represent the percentage of ice-shelf area within each bin. (b) Basal mass budget integrated from shallow to deep ice shelf drafts for 50 m bins of ice draft. (c) Averaged rates of basal ice thickness change as a function of distance from the ice-shelf front at a bin size of 10 km.

### 5.3. Spatial Distribution of Basal Melting and Freezing

The spatial patterns of the basal mass budgets confirm that the largest melt rates occur near the deep grounding lines of the major ice streams (Figures 10 and 11a). For these large ice shelves, high basal melt rates near the grounding lines are associated with flow into the sub-ice-shelf cavity of dense, high-salinity shelf water (HSSW) with temperature near the local surface freezing point of approximately  $-1.9^{\circ}\text{C}$ : the HSSW is formed on the broad continental shelves seaward of the ice fronts by cooling and brine rejection during sea-ice formation in winter [Nicholls *et al.*, 1991; Jacobs *et al.*, 1992]. The HSSW, although cold, is warm relative to the pressure-dependent freezing point of seawater ( $T_f(S,P)$ , where  $S$  is salinity and  $P$  is pressure), which decreases with increasing  $P$  ( $\sim-2.65^{\circ}\text{C}$  at 1000 m). Therefore, the ocean thermal forcing ( $\propto(T - T_f)$ ) increases as ice draft deepens, and we expect more rapid melting.

The low-density meltwater produced by ice melt near the grounding line mixes with ambient seawater and rises along the ice shelf draft and may become supercooled with the potential to form frazil ice crystals that accrete to the ice-shelf base as marine ice [Oerter *et al.*, 1992]. This “ice-pump” mechanism [Lewis and Perkin, 1986] is most evident on FRIS (Figure 10b) along the outflow of Foundation Ice Stream where we find melt rates in excess of  $5 \text{ m a}^{-1}$  in a 50 km zone close to the grounding line, in agreement with ground measurements [Lambrecht *et al.*, 1999], and strong basal freezing ( $1\text{--}2 \text{ m a}^{-1}$ ) along an ice-flow divergence zone (Figure 9d) on the northeastern side of Henry Ice Rise. This pronounced accretion zone has previously been inferred from volume-flux divergence calculations [Joughin and Padman, 2003] and is responsible for building up a thick marine ice layer ( $<500 \text{ m}$ ) that extends all the way to the ice-shelf front [Joughin and Vaughan, 2004], comparable to the basal accumulation pattern on Amery Ice Shelf [Fricker *et al.*, 2001]. We observe a slight Eulerian-derived surface lowering over this accretion zone ( $30\text{--}40 \text{ mm a}^{-1}$  on average, Figure 3e), which suggests that recent freezing rates are 20–30% lower than balanced conditions, but we cannot exclude residual impacts from, for example, changes in firn air content. The Lagrangian-derived elevation changes over the same area (Figure 3f) are masked by the missing ice advection, but the anomalously high variability (Figure 3h) indicates that there might be significant temporal variations in freezing rates.

Other zones of strong basal freezing ( $>1 \text{ m a}^{-1}$ ) on FRIS are the southeastern faces of Cape Zumberge and Fowler Peninsula on the western side of Ronne Ice Shelf, and along the east side of Berkner Island toward the Filchner ice front (Figure 10b). Airborne radio-echo sounding data [Lambrecht *et al.*, 2007] have revealed elongated bands of thick marine ice (100–400 m) downstream of all these zones (Figure 2d). The dominant sources of supercooled water on the western side of FRIS are likely the deep grounding zones of the Evans and Rutherford Ice Streams where high basal melt rates ( $>4 \text{ m a}^{-1}$ ) have also been measured previously [Jenkins and Doake, 1991; Rignot and Jacobs, 2002; Joughin and Padman, 2003]. On RIS, only Byrd Glacier shows pronounced melting near the grounding zone (Figure 10a). The remainder of RIS has only weak patterns of melting and freezing that are close to the noise level of the observations. Formation of marine ice layers is difficult to predict from these results, but they are known to exist [Zotikov *et al.*, 1980] and may extend over

substantial areas although the fraction of the total ice volume is small [Griggs and Bamber, 2011]. The lower magnitude and variability of basal processes for RIS can be attributed to its shallower and more uniform ice draft; the shallower draft reduces the thermal contrast between the ocean temperature and the in situ freezing point, and the uniformity reduces lateral spreading. The generally stronger tidal currents under FRIS [Makinson et al., 2011], relative to RIS [MacAyeal, 1984], may also influence the basal conditions.

Relatively strong basal melting also occurs toward the ice fronts (the so-called “ice shelf frontal zone”) on both ice shelves (Figures 10 and 11c), where seasonally warmed surface waters can reach the shallower parts of the ice shelf draft through forcing from winds and tides [Jacobs et al., 1979, 1992]. Horgan et al. [2011] analyzed ICESat repeat-track data using a Lagrangian approach over the frontal zone of RIS and found this increase to be exponential with peak rates of  $\sim 3 \text{ m a}^{-1}$  close to the ice front. Our processing method does not have the spatial resolution to resolve melt rates all the way to the ice fronts, but we obtain average melt rates of  $0.8 \text{ m a}^{-1}$  for the seaward 10 km of RIS (Figure 11c). This value is about half that obtained from moorings deployed for  $\sim 2$  months in summer 2010–2011,  $\sim 6$  and  $\sim 16$  km south of the ice front east of Ross Island [Arzeno et al., 2014]. The melt rates in the FRIS frontal zone vary from up to  $5 \text{ m a}^{-1}$  ( $1.6 \text{ m a}^{-1}$  on average) along the Ronne ice front to a narrow zone of freezing along the much thicker Filchner ice front (Figures 10b and 2d), which is consistent with previous studies [Jenkins and Doake, 1991; Joughin and Padman, 2003] and also are reflected in the overall relation between basal mass budget and ice shelf draft (Figures 11a and 11b).

Integrating the basal melt rates over the outermost 100 km of each ice shelf (Figure 11c), we find that these frontal zones account for  $\sim 50\%$  and  $\sim 40\%$  of the total basal melting of RIS and FRIS, respectively. For comparison, the closest 100 km of the grounding line of all main ice streams of FRIS accounts for  $\sim 40\%$  of its total melting. The frontal zones are more directly coupled to nearby wind patterns, air temperatures, and sea-ice cover [Stern et al., 2013; Arzeno et al., 2014]; therefore, they might be more susceptible to climatic change than the deep grounding zones where the thermohaline circulation is believed to be relatively stable and might even slow down in a warming climate as reduced sea ice production reduces the HSSW formation rate [Nicholls, 1997]. This is in contrast to the Amundsen Sea sector where warm Circumpolar Deep Water is able to reach the ice-shelf grounding lines and cause rapid basal melting with freshwater fluxes that far exceed those from near the ice front [Rignot et al., 2013].

## 6. Conclusions and Outlook

We have performed consistent analyses of Eulerian and Lagrangian elevation changes using ICESat satellite laser altimeter for the period 2003–2009 over the two largest ice shelves in Antarctica: Ross and Filchner-Ronne (RIS and FRIS). Local Eulerian elevation changes are dominated by advection of surface undulations with short spatial scales. Lagrangian processing using an external velocity field allows us to reduce the contribution of surface roughness by comparing elevations at topographically consistent locations. This method produces more spatially coherent patterns of elevation change that can be used to interpret the oceanic and atmospheric contributions to the ice-shelf mass budgets. The maps of Lagrangian elevation changes can be converted into maps of basal mass budget as the residual after accounting for changing ocean conditions, firn air content, surface accumulation, and ice-flow divergence.

Both the RIS and FRIS are close to steady state conditions, although their basal mass budgets have different characteristics. Integrating the basal mass budgets over the ice shelf areas, we obtain net estimates of  $-50 \pm 64 \text{ Gt a}^{-1}$  for RIS and  $-124 \pm 66 \text{ Gt a}^{-1}$  for FRIS, consistent with previous studies that are based on ice fluxes at the ice-shelf perimeters and modeled surface mass budgets. On FRIS, rapid melting occurs near the deep grounding lines of the tributary ice streams; however, much of this melt is offset by significant basal freezing (marine ice accretion) in downstream zones with strong lateral spreading. In contrast, RIS has lower melting near the grounding lines and no pronounced zones of marine ice formation; we hypothesize that this is due to the shallower and more uniform ice draft and, potentially, also the relatively weak tidal currents. Both ice shelves show a clear pattern of increased basal melting towards their ice fronts, and we find that one third to one half of the total basal melting occurs within the seaward 100 km of the ice shelves.

In the case of near steady state ice shelves like RIS and FRIS, the success of future applications of similar methods is highly dependent on direct observations or improved modeling of changes in the firn pack. We find that deviations between existing estimates of net mass budget for RIS and FRIS within the last two

decades are likely more related to inconsistent modeled firn corrections than to actual temporal variation. We have presented an indirect method of estimating firn-pack changes based on elevation changes over ice rises and the grounded ice sheet. This may be a viable alternative to firn-pack modeling, especially in areas where the climatological input data are poorly constrained.

Our study focused on RIS and FRIS because Lagrangian analysis of ICESat data was not successful for the smaller Antarctic ice shelves at lower latitudes with sparser track spacing that results in relatively few comparable neighbor points being found after velocity-based translation of ground tracks. This will likely improve with the denser track-coverage of modern satellite altimeters like CryoSat-2 and ICESat-2, potentially also allowing simultaneous derivation of ice-flow velocity and divergence through topographic matching of surface features within patches of altimeter tracks.

### Acknowledgments

The authors are thankful to the numerous contributors that made their data publicly available: NASA/NSIDC (ICESat data), the IPY-MEaSURES program (velocity maps and grounding lines), ASAID (grounding lines), MOA (ice fronts), DTU Space (mean dynamic topography), and AVISO (sea level change). We thank S.R.M. Ligtenberg, J.T.M. Lenaerts, and M.v.d. Broeke (Utrecht University) for providing firn thickness corrections and for constructive discussions about firn-pack changes. We thank B. Scheuchl and two anonymous reviewers for their valuable comments on the original manuscript. This study was supported by funding from NASA grants NNX10AG19G and NNX12AH16G. This is ESR contribution 153 (assigned on acceptance).

### References

- Abdalati, W., et al. (2010), The ICESat-2 laser altimetry mission, *Proc. IEEE*, 98, 735–751, doi:10.1109/jproc.2009.2034765.
- Abshire, J. B., X. L. Sun, H. Irisi, J. M. Sirota, J. F. McGarry, S. Palm, D. H. Yi, and P. Liiva (2005), Geoscience Laser Altimeter System (GLAS) on the ICESat mission: On-orbit measurement performance, *Geophys. Res. Lett.*, 32, L21S02, doi:10.1029/2005GL024028.
- Andersen, O. B., P. Knudsen, and L. Stenseng (2013), The DTU13 global mean sea surface from 20 years of satellite altimetry, OSTST Meeting, Boulder, Colo., Oct. 2013.
- Arzeno, I. B., R. C. Beardsley, R. Limeburner, B. Owens, L. Padman, S. R. Springer, C. L. Stewart, and M. J. M. Williams (2014), Ocean variability contributing to basal melt rate near the ice front of Ross Ice Shelf, Antarctica, *J. Geophys. Res. Oceans*, 119, 4214–4233, doi:10.1002/2014JC009792.
- Bindschadler, R., et al. (2011), Getting around Antarctica: New high-resolution mappings of the grounded and freely-floating boundaries of the Antarctic ice sheet created for the International Polar Year, *Cryosphere*, 5, 569–588, doi:10.5194/tc-5-569-2011.
- Bintanja, R., G. J. van Oldenborgh, S. S. Drijfhout, B. Wouters, and C. A. Katsman (2013), Important role for ocean warming and increased ice-shelf melt in Antarctic sea-ice expansion, *Nat. Geosci.*, 6, 376–379, doi:10.1038/ngeo1767.
- Borsa, A. A., G. Moholdt, H. A. Fricker, and K. M. Brunt (2013), A range correction for ICESat and its potential impact on ice-sheet mass balance studies, *Cryosphere*, 8, doi:10.5194/tc-8-1-2014.
- Brunt, K. M., H. A. Fricker, L. Padman, T. A. Scambos, and S. O’Neal (2010), Mapping the grounding zone of the Ross Ice Shelf, Antarctica, using ICESat laser altimetry, *Ann. Glaciol.*, 51, 71–79, doi:10.3189/172756410791392790.
- Brunt, K. M., H. A. Fricker, and L. Padman (2011), Analysis of ice plains of the Filchner-Ronne Ice Shelf, Antarctica, using ICESat laser altimetry, *J. Glaciol.*, 57, 965–975, doi:10.3189/172756410791392790.
- Chelton, D. B., and D. B. Enfield (1986), Ocean signals in tide-gauge records, *J. Geophys. Res.*, 91, 9081–9098, doi:10.1029/JB091iB09p09081.
- Depoorter, M. A., J. L. Bamber, J. A. Griggs, J. T. M. Lenaerts, S. R. M. Ligtenberg, M. R. van den Broeke, and G. Moholdt (2013), Calving fluxes and basal melt rates of Antarctic ice shelves, *Nature*, 502(7469), 89–93, doi:10.1038/nature12567.
- Dupont, T. K., and R. B. Alley (2005), Assessment of the importance of ice-shelf buttressing to ice-sheet flow, *Geophys. Res. Lett.*, 32, L04503, doi:10.1029/2004GL022024.
- Dutrieux, P., D. G. Vaughan, H. F. J. Corr, A. Jenkins, P. R. Holland, I. Joughin, and A. Fleming (2013), Pine Island Glacier ice shelf melt distributed at kilometre scales, *Cryosphere Discuss.*, 7, 1591–1620, doi:10.5194/tcd-7-1591-2013.
- Favier, V., C. Agosta, S. Parouty, G. Durand, G. Delaygue, H. Gallée, A. S. Drouet, A. Trouvilliez, and G. Krinner (2013), An updated and quality controlled surface mass balance dataset for Antarctica, *Cryosphere*, 7, 583–597, doi:10.5194/tc-5197-5583-2013.
- Foster, T. D. (1983), The temperature and salinity fine-structure of the ocean under the Ross Ice Shelf, *J. Geophys. Res.*, 88, 2556–2564, doi:10.1029/JC088iC04p02556.
- Fretwell, P., et al. (2013), Bedmap2: Improved ice bed, surface and thickness datasets for Antarctica, *Cryosphere*, 7, 375–393, doi:10.5194/tc-7-375-2013.
- Fricker, H. A., and L. Padman (2012), Thirty years of elevation change on Antarctic Peninsula ice shelves from multimission satellite radar altimetry, *J. Geophys. Res.*, 117, C02026, doi:10.1029/2011JC007126.
- Fricker, H. A., S. Popov, I. Allison, and N. Young (2001), Distribution of marine ice beneath the Amery Ice Shelf, *Geophys. Res. Lett.*, 28, 2241–2244, doi:10.1029/2000GL012461.
- Fricker, H. A., J. N. Bassis, B. Minster, and D. R. MacAyeal (2005a), ICESat’s new perspective on ice shelf rifts: The vertical dimension, *Geophys. Res. Lett.*, 32, L23S08, doi:10.1029/2005GL025070.
- Fricker, H. A., A. Borsa, B. Minster, C. Carabajal, K. Quinn, and B. Bills (2005b), Assessment of ICESat performance at the Salar de Uyuni, Bolivia, *Geophys. Res. Lett.*, 32, L21S06, doi:10.1029/2005GL023423.
- Graf, W., O. Reinwarth, H. Oerter, C. Mayer, and A. Lambrecht (1999), Surface accumulation on foundation ice stream, Antarctica, *Ann. Glaciol.*, 29, 23–28, doi:10.3189/172756499781820987.
- Griggs, J. A., and J. L. Bamber (2011), Antarctic ice-shelf thickness from satellite radar altimetry, *J. Glaciol.*, 57, 485–498, doi:10.3189/002214311796905659.
- Gunter, B. C., O. Didova, R. E. M. Riva, S. R. M. Ligtenberg, J. T. M. Lenaerts, M. A. King, M. R. van den Broeke, and T. Urban (2013), Empirical estimation of present-day Antarctic glacial isostatic adjustment and ice mass change, *Cryosphere Discuss.*, 7, 3497–3541, doi:10.5194/tcd-7-3497-2013.
- Haug, T., A. Kääb, and P. Skvarca (2010), Monitoring ice shelf velocities from repeat MODIS and Landsat data—A method study on the Larsen C ice shelf, Antarctic Peninsula, and 10 other ice shelves around Antarctica, *Cryosphere*, 4, 161–178, doi:10.5194/tc-4-161-2010.
- Hellmer, H. H. (2004), Impact of Antarctic ice shelf basal melting on sea ice and deep ocean properties, *Geophys. Res. Lett.*, 31, L10307, doi:10.1029/2004GL019506.
- Hellmer, H. H., F. Kauker, R. Timmermann, J. Determann, and J. Rae (2012), Twenty-first-century warming of a large Antarctic ice-shelf cavity by a redirected coastal current, *Nature*, 485, doi:10.1038/nature11064.
- Helsen, M. M., M. R. van den Broeke, R. S. W. van de Wal, W. J. van de Berg, E. van Meijgaard, C. H. Davis, Y. H. Li, and I. Goodwin (2008), Elevation changes in Antarctica mainly determined by accumulation variability, *Science*, 320, 1626–1629, doi:10.1126/science.1153894.
- Hofton, M. A., S. B. Luthcke, and J. B. Blair (2013), Estimation of ICESat intercampaign elevation biases from comparison of lidar data in East Antarctica, *Geophys. Res. Lett.*, 40, 5698–5703, doi:10.1002/2013GL057652.

- Horgan, H. J., R. T. Walker, S. Anandakrishnan, and R. B. Alley (2011), Surface elevation changes at the front of the Ross Ice Shelf: Implications for basal melting, *J. Geophys. Res.*, 116, C02005, doi:10.1029/2010JC006192.
- Hulbe, C. L., T. A. Scambos, C.-K. Lee, J. Bohlander, and T. Haran (2013), Recent changes in the flow of the Ross Ice Shelf, West Antarctica, *Earth Planet. Sci. Lett.*, 376, 54–62, doi:10.1016/j.epsl.2013.06.013.
- Jacobs, S. S., and C. F. Giulivi (2010), Large multidecadal salinity trends near the Pacific-Antarctic continental margin, *J. Clim.*, 23, 4508–4524, doi:10.1175/2010jcli3284.1.
- Jacobs, S. S., A. L. Gordon, and J. L. Arda (1979), Circulation and melting beneath the Ross Ice Shelf, *Science*, 203, 439–443.
- Jacobs, S. S., D. R. Macayeal, and J. L. Arda (1986), The recent advance of the Ross Ice Shelf, Antarctica, *J. Glaciol.*, 32, 464–474.
- Jacobs, S. S., H. H. Helmer, C. S. M. Doake, A. Jenkins, and R. M. Frolich (1992), Melting of ice shelves and the mass balance of Antarctica, *J. Glaciol.*, 38, 375–387.
- Jenkins, A., and C. S. M. Doake (1991), Ice-ocean interaction on Ronne Ice Shelf, Antarctica, *J. Geophys. Res.*, 96, 791–813, doi:10.1029/90JC01952.
- Jezek, K., and RAMP Product Team (2002), RAMP AMM-1 SAR Image Mosaic of Antarctica, Fairbanks, AK: Alaska SAR Facility, in association with the Natl. Snow and Ice Data Cent., Boulder, Colo., Digital media.
- Joughin, I., and L. Padman (2003), Melting and freezing beneath Filchner-Ronne Ice Shelf, Antarctica, *Geophys. Res. Lett.*, 30(9), 1477, doi:10.1029/2003GL016941.
- Joughin, I., and D. G. Vaughan (2004), Marine ice beneath the Filchner-Ronne Ice Shelf, Antarctica: A comparison of estimated thickness distributions, *Ann. Glaciol.*, 39, 511–517, doi:10.3189/172756404781814717.
- Joughin, I., R. B. Alley, and D. M. Holland (2012), Ice-sheet response to oceanic forcing, *Science*, 338, 1172–1176, doi:10.1126/science.1226481.
- Khazendar, A., and A. Jenkins (2003), A model of marine ice formation within Antarctic ice shelf rifts, *J. Geophys. Res.*, 108(C7), 3235, doi:10.1029/2002JC001673.
- Korona, J., E. Berthier, M. Bernard, F. Remy, and E. Thouvenot (2009), SPIRIT. SPOT 5 stereoscopic survey of Polar Ice: Reference Images and Topographies during the fourth International Polar Year (2007–2009), *ISPRS J. Photogramm.*, 64, 204–212, doi:10.1016/j.isprsjprs.2008.10.005.
- Kusahara, K., and H. Hasumi (2013), Modeling Antarctic ice shelf responses to future climate changes and impacts on the ocean, *J. Geophys. Res. Oceans*, 118, 2454–2475, doi:10.1002/jgrc.20166.
- Lambrecht, A., C. Mayer, H. Oerter, and U. Nixdorf (1999), Investigations of the mass balance of the southeastern Ronne Ice Shelf, Antarctica, *Ann. Glaciol.*, 29, 250–254, doi:10.3189/172756499781820996.
- Lambrecht, A., H. Sandhäger, D. G. Vaughan, and C. Mayer (2007), New ice thickness maps of Filchner-Ronne Ice Shelf, Antarctica, with specific focus on grounding lines and marine ice, *Antarct. Sci.*, 19, 521–532, doi:10.1017/S0954102007000661.
- Lazzara, M. A., K. C. Jezez, T. A. Scambos, D. R. MacAyeal, and C. J. Van Der Veen (2008), On the recent calving of icebergs from the Ross ice shelf, *Polar Geog.*, 31(1–2), 15–26, doi:10.1080/10889370802175937.
- Le Traon, P. Y., F. Nadal, and N. Ducet (1998), An improved mapping method of multisatellite altimeter data, *J. Atmos. Oceanic Technol.*, 15(2), 522–534, doi:10.1175/1520-0426(1998)015.
- Lee, C. K., K. W. Seo, S. C. Han, J. Yu, and T. A. Scambos (2012), Ice velocity mapping of Ross Ice Shelf, Antarctica by matching surface undulations measured by ICESat laser altimetry, *Remote Sens. Environ.*, 124, 251–258, doi:10.1016/j.rse.2012.05.017.
- Lenarts, J. T. M., M. R. van den Broeke, W. J. van de Berg, E. van Meijgaard, and P. K. Munnink (2012), A new, high-resolution surface mass balance map of Antarctica (1979–2010) based on regional atmospheric climate modeling, *Geophys. Res. Lett.*, 39, L04501, doi:10.1029/2011GL050713.
- Lewis, E. L., and R. G. Perkin (1986), Ice pumps and their rates, *J. Geophys. Res.*, 91, 1756–1762, doi:10.1029/JC091iC10p11756.
- Ligtenberg, S. R. M., M. M. Helsen, and M. R. van den Broeke (2011), An improved semi-empirical model for the densification of Antarctic firn, *Cryosphere*, 5, 809–819, doi:10.5194/tc-5-809-2011.
- MacAyeal, D. R. (1984), Numerical simulations of the Ross Sea tides, *J. Geophys. Res.*, 89, 607–615, doi:10.1029/JC089iC01p00607.
- Mahesh, A., J. D. Spinharine, D. P. Duda, and E. W. Eloranta (2002), Atmospheric multiple scattering effects on GLAS altimetry. Part II: Analysis of expected errors in antarctic altitude measurements, *IEEE Trans. Geosci. Remote*, 40, 2353–2362, doi:10.1109/tgrs.2002.803849.
- Makinson, K., P. R. Holland, A. Jenkins, K. W. Nicholls, and D. M. Holland (2011), Influence of tides on melting and freezing beneath Filchner-Ronne Ice Shelf, Antarctica, *Geophys. Res. Lett.*, 38, L06601, doi:10.1029/2010GL046462.
- Marsh, O. J., and W. Rack (2012), A method of calculating ice-shelf surface velocity using ICESat altimetry, *Polar Rec.*, 48, 25–30, doi:10.1017/s0032247411000362.
- Martin, S., R. S. Drucker, and R. Kwok (2007), The areas and ice production of the western and central Ross Sea polynyas, 1992–2002, and their relation to the B-15 and C-19 iceberg events of 2000 and 2002, *J. Mar. Syst.*, 68, 201–214, doi:10.1016/j.jmarsys.2006.11.008.
- Medley, B., et al. (2013), Airborne-radar and ice-core observations of annual snow accumulation over Thwaites Glacier, West Antarctica confirm the spatiotemporal variability of global and regional atmospheric models, *Geophys. Res. Lett.*, 40, 3649–3654, doi:10.1002/grl.50706.
- Menemenlis, D., J. Campin, P. Heimbach, C. Hill, T. Lee, A. Nguyen, M. Schodlok, and H. Zhang (2008), ECCO2: High resolution global ocean and sea ice data synthesis, *Mercator Ocean Q. Newslet.*, 31, 13–21.
- Nicholls, K. W. (1997), Predicted reduction in basal melt rates of an Antarctic ice shelf in a warmer climate, *Nature*, 388, 460–462.
- Nicholls, K. W., and K. Makinson (1985), Ocean circulation beneath the Western Ronne Ice Shelf, as derived from in situ measurements of water currents and properties, *Antarct. Res. Ser.*, 75, 301–318, doi:10.1029/AR075p0301.
- Nicholls, K. W., K. Makinson, and A. V. Robinson (1991), Ocean circulation beneath the Ronne ice shelf, *Nature*, 354, 221–223, doi:10.1038/354221a0.
- Nicholls, K. W., K. Makinson, and M. R. Johnson (1997), New oceanographic data from beneath Ronne Ice Shelf, Antarctica, *Geophys. Res. Lett.*, 24, 167–170, doi:10.1029/96GL03922.
- Oerter, H., J. Kipfstuhl, J. Determann, H. Miller, D. Wagenbach, A. Minikin, and W. Graf (1992), Evidence for basal marine ice in the Filchner-Ronne Ice Shelf, *Nature*, 358, 399–401, doi:10.1038/358399a0.
- Padman, L., H. A. Fricker, R. Coleman, S. Howard, and L. Erofeeva (2002), A new tide model for the Antarctic ice shelves and seas, *Ann. Glaciol.*, 34, 247–254, doi:10.3189/172756402781817752.
- Padman, L., M. King, D. Goring, H. Corr, and R. Coleman (2003), Ice-shelf elevation changes due to atmospheric pressure variations, *J. Glaciol.*, 49, 521–526, doi:10.3189/172756503781830386.
- Padman, L., et al. (2012), Oceanic controls on the mass balance of Wilkins Ice Shelf, Antarctica, *J. Geophys. Res.*, 117, C01010, doi:10.1029/2011JC007301.
- Pritchard, H. D., S. R. M. Ligtenberg, H. A. Fricker, D. G. Vaughan, M. R. van den Broeke, and L. Padman (2012), Antarctic ice-sheet loss driven by basal melting of ice shelves, *Nature*, 484, doi:10.1038/nature10968.
- Rignot, E., and S. S. Jacobs (2002), Rapid bottom melting widespread near Antarctic ice sheet grounding lines, *Science*, 296, 2020–2023, doi:10.1126/science.1070942.
- Rignot, E., J. Mouginot, and B. Scheuchl (2011a), Ice flow of the antarctic ice sheet, *Science*, 333, 1427–1430, doi:10.1126/science.1208336.

- Rignot, E., J. Mouginot, and B. Scheuchl (2011b), Antarctic grounding line mapping from differential satellite radar interferometry, *Geophys. Res. Lett.*, 38, L10504, doi:10.1029/2011GL047109.
- Rignot, E., S. Jacobs, J. Mouginot, and B. Scheuchl (2013), Ice-shelf melting around Antarctica, *Science*, 341, 266–270, doi:10.1126/science.1235798.
- Roemmich, D., and J. Gilson (2009), The 2004–2008 mean and annual cycle of temperature, salinity, and steric height in the global ocean from the Argo Program, *Prog. Oceanogr.*, 82, 81–100, doi:10.1016/j.pocean.2009.03.004.
- Rye, C. D., A. C. Naveira Garabato, P. R. Holland, M. P. Meredith, A. J. George Nurser, C. W. Hughes, A. C. Coward, and D. J. Webb (2014), Rapid sea-level rise along the Antarctic margins in response to increased glacial discharge, *Nat. Geosci.*, 7, 732–735, doi:10.1038/ngeo2230.
- Scambos, T. A., T. M. Haran, M. A. Fahnestock, T. H. Painter, and J. Bohlander (2007), MODIS-based Mosaic of Antarctica (MOA) data sets: Continent-wide surface morphology and snow grain size, *Remote Sens. Environ.*, 111, 242–257, doi:10.1016/j.rse.2006.12.020.
- Scheuchl, B., J. Mouginot, and E. Rignot (2012), Ice velocity changes in the Ross and Ronne sectors observed using satellite radar data from 1997 and 2009, *Cryosphere*, 6, 1019–1030, doi:10.5194/tc-6-1019-2012.
- Schutz, B. E., H. J. Zwally, C. A. Shuman, D. Hancock, and J. P. DiMarzio (2005), Overview of the ICESat Mission, *Geophys. Res. Lett.*, 32, L21501, doi:10.1029/2005GL024009.
- Shepherd, A., D. Wingham, T. Payne, and P. Skvarca (2003), Larsen ice shelf has progressively thinned, *Science*, 302, 856–859, doi:10.1126/science.1089768.
- Shepherd, A., D. Wingham, T. Payne, and P. Skvarca (2004), Correction to “Larsen ice shelf has progressively thinned”, *Science*, 303, 1612.
- Shepherd, A., D. Wingham, D. Wallis, K. Giles, S. Laxon, and A. V. Sundal (2010), Recent loss of floating ice and the consequent sea level contribution, *Geophys. Res. Lett.*, 37, L13503, doi:10.1029/2010GL042496.
- Smith, B. E., C. R. Bentley, and C. F. Raymond (2005), Recent elevation changes on the ice streams and ridges of the Ross Embayment from ICESat crossovers, *Geophys. Res. Lett.*, 32, L21509, doi:10.1029/2005GL024365.
- Smith, B. E., H. A. Fricker, I. R. Joughin, and S. Tulaczyk (2009), An inventory of active subglacial lakes in Antarctica detected by ICESat (2003–2008), *J. Glaciol.*, 55, 573–595, doi:10.3189/002214309789470879.
- Stern, A. A., M. S. Dinniman, V. Zagorodnov, S. W. Tyler, and D. M. Holland (2013), Intrusion of warm surface water beneath the McMurdo Ice Shelf, Antarctica, *J. Geophys. Res. Oceans*, 118, 7036–7048, doi:10.1002/2013JC008842.
- Timmermann, R., Q. Wang, and H. H. Hellmer (2012), Ice-shelf basal melting in a global finite-element sea-ice/ice-shelf/ocean model, *Ann. Glaciol.*, 53, 303–314, doi:10.3189/2012AoG60A156.
- van der Veen, C. J. (1986), Numerical modeling of ice shelves and ice tongues, *Ann. Geophys.*, 4, 45–53.
- Vaughan, D. G., J. L. Bamber, M. Giovinetto, J. Russell, and A. P. R. Cooper (1999), Reassessment of net surface mass balance in Antarctica, *J. Clim.*, 12, 933–946, doi:10.1175/1520-0442(1999)012.
- Vaughan, D. G., H. F. J. Corr, R. A. Bindschadler, P. Dutrieux, G. H. Gudmundsson, A. Jenkins, T. Newman, P. Vornberger, and D. J. Wingham (2012), Subglacial melt channels and fracture in the floating part of Pine Island Glacier, Antarctica, *J. Geophys. Res.*, 117, F03012, doi:10.1029/2012JF002360.
- Wingham, D. J., et al. (2006), CryoSat: A mission to determine the fluctuations in Earth's land and marine ice fields, *Nat. Hazard. Oceanogr. Process. Satell. Data*, 37, 841–871, doi:10.1016/j.asr.2005.07.027.
- Zotikov, I. A., V. S. Zagorodnov, and J. V. Raikovsky (1980), Core drilling through the Ross Ice Shelf (Antarctica) confirmed basal freezing, *Science*, 207, 1463–1465, doi:10.1126/science.207.4438.1463.
- Zwally, H. J., and M. B. Giovinetto (1995), Accumulation in Antarctica and Greenland derived from passive-microwave data: A comparison with contoured compilations, *Ann. Glaciol.*, 21, 123–130.
- Zwally, H. J., M. B. Giovinetto, J. Li, H. G. Cornejo, M. A. Beckley, A. C. Brenner, J. L. Saba, and D. H. Yi (2005), Mass changes of the Greenland and Antarctic ice sheets and shelves and contributions to sea-level rise: 1992–2002, *J. Glaciol.*, 51, 509–527, doi:10.3189/172756505781829007.
- Zwally, H. J., M. B. Giovinetto, M. A. Beckley, and J. L. Saba (2012), Antarctic and Greenland Drainage Systems. [Available at [http://icesat4.gsfc.nasa.gov/cryo\\_data/ant\\_grn\\_drainage\\_systems.php](http://icesat4.gsfc.nasa.gov/cryo_data/ant_grn_drainage_systems.php).]